

**EFFECT OF THE WIDTH AND NUMBER OF RINGS IN A
CONCENTRIC SPLIT RING RESONATOR ON PLASMA
GENERATION FOR MINIATURE ION THRUSTER**

by

NAGESHWAR NAGARAJAN

A THESIS

**Submitted in partial fulfillment of the requirements
for the degree of Master of Science
in
The Department of Mechanical and Aerospace Engineering
to
The School of Graduate Studies
of
The University of Alabama in Huntsville**

HUNTSVILLE, ALABAMA

2021

ABSTRACT

The School of Graduate Studies
The University of Alabama in Huntsville

Degree Master of Science College/Dept. Engineering/Mechanical and
Aerospace Engineering

Name of Candidate Nageshwar Nagarajan

Title Effect of the Width and Number of Rings in a Concentric Split Ring Resonator
on Plasma Generation for Miniature Ion Thruster

The objective of this thesis is to study the plasma generated by concentric split ring resonators used in miniature ion engines. Multiple resonators were designed and built with two or three concentric rings and different ring widths. Five different designs of the resonator were tested. The concentric split ring resonators are first tested at 350 mTorr with argon gas at an average 7.25 W forward power. The plasma density and electron temperature produced by the resonators were mapped in a 2D plane using double Langmuir probes. All the designs were placed into a miniature ion thruster and the thruster performance was measured. The 2 ringed thinner inner ring split ring resonator performed better than the other designs in both plasma properties and thrust. The thrust for the best design ranged from 1.58 μN to 2.34 μN and the specific impulse was 2662 seconds.

Abstract Approval: Committee Chair _____
Dr. Kunning G. Xu

Department Chair _____
Dr. Keith Hollingsworth

Graduate Dean _____
Dr. Jon Hakkila

ACKNOWLEDGEMENTS

I would like to thank Dr. Gabe Xu for his suggestion of the research topic and for his guidance through the stages of the work. I would also like to thank the MAE department for providing me assistantship and taking the financial burden off my shoulders.

I would also like to thank my family and friends who supported me throughout my graduate studies. I'd also like to thank my PERL lab mates: Andrew for helping me figure out everything in the PERL lab from operating the vacuum chamber to finding the right size of the wrench; Neil for his instructions on fabricating the CSRR and operating the 3D printer; and Zach for his moral support and his wits that made the lab environment more comfortable for me to adapt. I would also like to thank Mr. Jon Buckley for fabricating the complex grid design with perfection on request. And finally, my thanks to God for keeping me at good health condition letting me complete this research without any interruption!

TABLE OF CONTENTS

LIST OF FIGURES	viii
LIST OF TABLES	x
LIST OF SYMBOLS	xi
CHAPTER 1. INTRODUCTION	1
1.1. Application in small satellites	2
1.2. Problem Statement	3
1.3. Research Contribution	3
CHAPTER 2. BACKGROUND	5
2.1. Plasma	5
2.2. Split Ring Resonators	6
2.3. SRR as a plasma source	8
2.4. Ion thruster	9
CHAPTER 3. EXPERIMENTAL METHODS	11
3.1. CSRR Design and Fabrication	11
3.2. Plasma Measurements	12
3.2.1. Facilities	12
3.2.2. Double Langmuir Probe	14
3.2.3. 2D Mapping and analysis	16
3.3. Thruster Setup	17
3.4. Neutralizer Cathode	20
CHAPTER 4. RESULTS AND DISCUSSION	21
4.1. Modeling and Test of CSRR	21

4.2. Plasma Mapping.....	24
4.3. Ion Thruster.....	28
4.4. Thrust Differences from Calculated to Actual.....	33
CHAPTER 5. CONCLUSION	35
REFERENCES.....	37
APPENDIX A: SURFACE PLOT	40

LIST OF FIGURES

Figure 1.1. Example of microwave propagation in SRR for current (blue) and voltage (red)	2
Figure 2.1 Split ring resonator device by Hopwood	6
Figure 2.2. Illustration of an electron bombardment ion thruster	9
Figure 3.1. Schematic of SRR (Left) and Fabricated SRR at UAH (Right)	11
Figure 3.2. The CAD designs	12
Figure 3.3. Experimental setup top-view for the CSRR plasma measurements	13
Figure 3.4. Schematic of double probe measurement. (a) voltage and current notation, (b) typical current-voltage characteristic	15
Figure 3.5. 11 x 11 grid of CSRR with probe at the 13 th position	16
Figure 3.6. CAD model of the thruster dissected and assembled isometric view	18
Figure 3.7. Working of the fabricated ion engine SRRIT2 (Right) and neutralizer cathode (Left) setup inside the vacuum chamber	19
Figure 3.8. Experimental setup of ion thruster	19
Figure 3.9. Schematic of Hollow Cathode[10]	20
Figure 4.1. S11 plot for 3-ringed constant width CSRR	22
Figure 4.2. The electric field simulation	23
Figure 4.3. Plasma generation	24
Figure 4.4. Surface plot of plasma number density of 3-ringed constant width CSRR	25
Figure 4.5. Surface plot of electron temperature of 3-ringed constant width CSRR	25
Figure 4.6. Thrust comparison plot at 4 SCCM mass flow rate.	30
Figure 4.7. Thrust comparison plot at 6 SCCM mass flow rate.	31
Figure 4.8. Thrust comparison plot at 8 SCCM mass flow rate.	31
Figure 4.9. Thrust comparison plot at 10 SCCM mass flow rate.	32
Figure A.1. Surface plot of plasma number density of 2-ringed 1 mm inner ring width CSRR ..	40

Figure A.2. Surface plot of electron temperature of 2-ringed 1 mm inner ring width CSRR	40
Figure A.3. Surface plot of plasma number density of 2-ringed 2 mm inner ring width CSRR ..	41
Figure A.4. Surface plot of electron temperature of 2-ringed 2 mm inner ring width CSRR	41
Figure A.5. Surface plot of plasma number density of 2-ringed constant width CSRR.....	42
Figure A.6. Surface plot of electron temperature of 2-ringed constant width CSRR.....	42
Figure A.7. Surface plot of plasma number density of 3-ringed constant width CSRR.....	43
Figure A.8. Surface plot of electron temperature of 3-ringed constant width CSRR.....	43
Figure A.9. Surface plot of plasma number density of 3-ringed varying width CSRR.....	44
Figure A.10. Surface plot of electron temperature of 3-ringed varying width CSRR.....	44

LIST OF TABLES

Table 1.1. Research question and methods table.....	4
Table 4.1. Resonant frequencies.....	22
Table 4.2. Measured CSRR plasma density and electron temperature results and theoretical thrust and Isp.....	27
Table 4.3. Updated Resonant Frequencies.....	29
Table 4.4. Power breakdown in the SRRIT2.....	33
Table 4.5. Pressure calculation parameters and values.....	34
Table 5.1 Conclusion.....	35

LIST OF SYMBOLS

SYMBOL	DEFINITION
c	<i>mean circumference of the ring</i>
ϵr	<i>dielectric constant of the material</i>
λ	<i>design frequency</i>
d	<i>mean diameter of the ring</i>
I	<i>current</i>
V	<i>voltage</i>
N_e	<i>plasma number density</i>
T_e	<i>electron temperature</i>
I_{sp}	<i>Specific Impulse</i>
I_b	<i>Beam current</i>
V_b	<i>Beam voltage</i>
T	<i>Thrust</i>
ηT	<i>Thruster efficiency</i>

CHAPTER 1. INTRODUCTION

This research focuses on how the concentric split ring resonators (CSRR) design affects the generated plasma properties. The CSRR is a device which can be used as a plasma source in an ion thruster. Ion thruster is an electrostatic thruster in which the ions are propelled to produce thrust using a pair of biased grids. The thrust produced is very low, on the order of μN and mN , but the specific impulse (I_{SP}) of the thruster will be very high. I_{SP} is a measure of a thruster's fuel efficiency, with higher values being better. Chemical rocket engines have maximum $I_{\text{SP}} \sim 450\text{-}500$ s, while ion thrusters can have $I_{\text{SP}} > 3000$ s. Due to its low thrust, ion thrusters are used in satellites for deep space missions and orbit maintenance where the high I_{SP} is desirable. For small satellites such as CubeSats, small scale and high I_{SP} propulsion devices are needed to provide orbit maintenance and orbit changes with minimal mass. Since small satellites have less electrical power, there is also a need for small and low power plasma sources for the ion thruster. One such device is the split ring resonator (SRR) which can generate plasma at power as low as 4.47 W.[1] When the microwave signal at the resonant frequency is applied to an SRR, electric fields with opposite directions are produced at the two ends of the split. Figure 1.1 shows the electric field generation. This opposite directional electric field creates a very high potential difference in the split gap which ionizes the gas around it. Higher input power and lower pressures increase the size of the plasma generated.

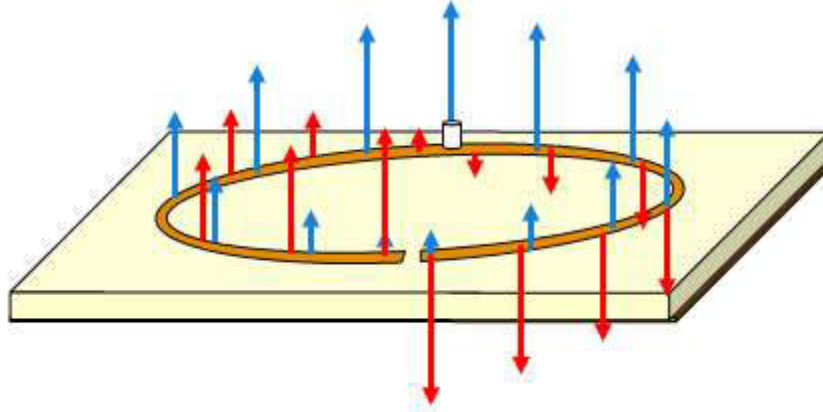


Figure 1.1. Example of microwave propagation in SRR for current (blue) and voltage (red)[2]

If additional rings are added inside the main ring, then a concentric split-ring resonator (CSRR) is formed. Since SRR and CSRR are small in size, they can act as an excellent source of plasma for miniature electric thrusters of small satellites. The SRR has been tested as a plasma generating device at the University of Alabama in Huntsville (UAH) for application to miniature ion engines. Since the plasma generated at the SRR is of higher density at the split, the distribution of plasma in the chamber is not uniform. By adding an extra ring, the plasma can be better distributed across the CSRR. The effect on the plasma density and electron temperature caused by different CSRR geometries such as increasing the number of rings and changing the width of the inner rings are analyzed in this research.

1.1. Application in small satellites

Smaller satellites are in demand in the space race in the current age. The communication satellites are getting smaller every decade so the propulsion systems have to adapt with the change. Starlink, the satellite internet constellation by SpaceX is a good example of need for small satellites.[3] Starlink is a network of smaller communication satellites in low earth orbit which aims to provide internet service all around the world. There are over 1,600 Starlink satellites in orbit currently. They are propelled by a krypton-fueled small Hall thruster. Smaller satellites

usually operate at lower powers due to smaller solar panels and batteries, so operating a high-power electric propulsion device can be challenging. A low powered miniaturized ion thruster can fill this need. The SRR can act as a good plasma source for miniaturized ion thruster due to its ability to generate high density plasma with low power.

1.2. Problem Statement

The SRR has been previously successfully tested as the plasma source in thruster by Yamauchi. However, the plasma is generated only at the one gap in the SRR, which creates a very non-uniform plasma, which in turn can cause a non-uniform and inefficient thruster. By adding a second ring, past work showed the CSRR provided a more uniform plasma than the SRR [2]. However, the design parameters of the CSRR which is responsible for the plasma properties were not studied defined in the past research. This research seeks to answer the following questions:

1. How is the CSRR plasma affected by changing the physical design of the CSRR?
2. How does changing the CSRR design in turn affect the performance of the ion thruster?

These questions are answered at the end of the research. This research focuses on the inner ring design parameter and the reaction to the plasma properties by varying the design parameters. This study examines the effects of the number of rings, and the width of the inner ring on the resulting plasma properties above concentric split ring resonators applicable to small space thrusters. The specific research questions and the hypothesis are given in Table 1.1.

1.3. Research Contribution

Previous research on SRR concluded that it can be a reliable low powered plasma source. The previous work by Yamauchi *et al.*[4] showed that the SRR can be used as a plasma source in ion thruster. Dextre *et al.*[2] analyzed the plasma properties of SRR and CSRR. The CSRR had evenly distributed electron temperature and less plasma density than the SRR but can be a better

source for ion thruster due to its evenly distributed plasma. This research will help in understanding the effect of CSRR design on the plasma properties such as plasma density and plasma temperature and help develop efficient designs which can produce more plasma with less power for a CSRR to use in the ion thruster.

Table 1.1. Research question and methods table.

Research Question	Hypothesis	Method	Publication
How do the additional rings of the CSRR affect the electric field and plasma distribution?	The more rings, the more evenly distributed plasma. But also, less plasma density due to the distributed electric field for the same power.	Analysis and experimental methods will be used. HFSS simulation will give the electric field distribution results. 2D – electron density mapping of CSRR will give the plasma density and plasma temperature.	Effect of the width and number of rings of concentric split ring resonator on plasma generation for miniature ion thruster. Will be converted into a technical journal paper in JPP.
How does increasing the number of rings affect the plasma?	By increasing the number of rings the distribution of electric field will be increased in turn loss of electric field strength will occur. Lower plasma density will be the result.	Testing the CSRR in the thruster gives the overall performance results and will validate the hypothesis. The two rings' and the 3 rings' 2D mapping results and the thruster results are compared.	
How does changing the width of the inner ring affect the plasma generation?	By decreasing the width of the inner ring, the electric field coupling will be made easier due to reduced area thus increasing the electric field strength. Thus, increase in plasma density. By increasing the width of the inner ring, the electric field coupling will require more power due to the increased area thus decreasing the electric field strength. Thus, decrease in plasma density.	The 2 rings 1 mm inner ring's and the 2 rings 2mm inner ring's 2D mapping results and the thruster results are compared.	

CHAPTER 2. BACKGROUND

2.1. Plasma

Plasma is produced by when a gas is excited to a sufficient high energy to be ionized. Ionization is the process of adding or removing electrons from neutral atoms and molecules to produce charged ions and electrons. Plasma is a gas that has a significant fraction of charged particles that are free to move in response to the electromagnetic fields they generate or externally applied fields. In a plasma, the number density of ion and electron are almost equal on a macroscopic scale, which is termed as ‘quasi-neutrality’. The condition is true throughout the plasma except at the boundaries. The quasi-neutrality is valid only if the spatial length of the plasma is larger than the Debye length. The Debye length is the characteristic length in which the charges or the boundaries are electrostatically shielded.

The most common properties that define the plasma are plasma number density (n_0) and electron temperature (T_e). The plasma number density can be either ion number density (n_i) or electron number density (n_e) as they both will be equal assuming quasi-neutrality. Electron temperature is the measure of the electron kinetic energy. The electron’s kinetic energy, along with the ionization barrier of the neutral atom or molecule determines the chance of ionization and creating a plasma. The higher the electron temperature, the greater the ionization rate. The electron temperature is usually expressed in electron Volts (eV) where $1 \text{ eV} = 11600 \text{ K}$. Plasma is used in many fields such as water purification[5], plasma detonation[6], fusion power[7], medical applications[8], food processing[8], plasma waste disposal (recycling)[9] and space application[10].

2.2. Split Ring Resonators

Split Ring Resonators (SRR) are metamaterials designed to filter microwave frequency signals.[11] The SRR consist of a conductive split ring on one side of a dielectric medium. The ring is designed for a specific resonant frequency. If the resonant frequency signal is passed to the SRR it acts as an antenna and receives the signal.[12] In turn if the ring is powered by a frequency generator at the design resonant frequency, then an electric field is generated in the split gap. If the electric field has enough energy, then ionization can occur in the discharge gap. SRRs can be easily and cheaply made using modern photolithography or circuit board milling techniques. An advantage of SRRs is its capability to operate at a range of wavelengths over the designed resonance configuration of the ring, allowing for frequency to control the plasma properties. The SRR is compact, and it can operate at very low power and a range of frequencies around the design resonant frequency. If the design resonant frequency increases, then the size of the ring decreases resulting in difficulty of fabrication. At resonance, a peak in plasma temperatures and densities is obtained. Figure 2.1 is a split ring resonator developed by Hopwood showing the relationship between the ring and a stem used for impedance matching[13], [14].

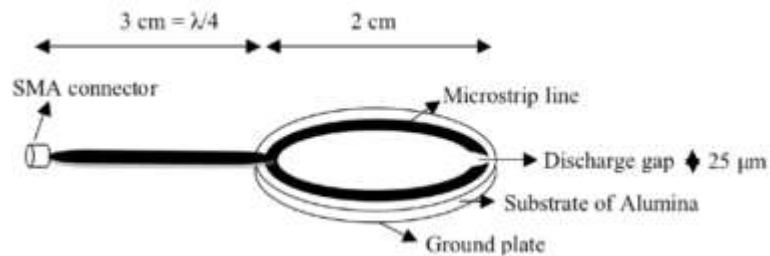


Figure 2.1 Split ring resonator device by Hopwood[14]

Overall, the purpose of these devices is to produce a desired electromagnetic response. Within the structure of the resonator, the electromagnetic flux induces oscillating currents, which follow the geometry of the resonator until it reaches the discharge gap. This leads to an incident field that is dependent on the resonant properties. An advantage of resonator technology is the ability to allow the

device to support resonant wavelengths other than the geometry of the ring. This would essentially expand the operating frequency of the resonator [14]; however, this trades off with the power required to operate the resonator. At off-resonant frequencies, more power is required. A second advantage of the SRR is its more compact structure compared to a linear resonator at the same frequency. This makes SRRs well-suited for small volume plasma generation such as in micro thrusters. SRRs can also generate higher plasma densities with less power than linear resonators [15]. The SRRs can operate over a wide range of frequencies, though the size of the ring shrinks significantly at very high frequencies and fabrication may become difficult.

To achieve ignition, the discharge gap potential of the SRR must be high enough to induce ionization. This can be described by a gap voltage equation developed by Iza [15]. This is given as,

$$V_{gap} = 4 \sqrt{\frac{Z_0 Q}{\pi}} \sqrt{P_{in}} \quad (2.1)$$

Here, Z_0 is the characteristic impedance, Q is the quality factor, and P_{in} is the input power. Typically, this occurs at the resonant frequency where the magnitude of the electric field in the discharge gap is optimal [1]. When operating at the resonant frequency, the impedance of the microwave system and SRR should match. This allows the corresponding microwave signal to deliver the maximum amount of power to the device and minimize any signal reflection [16]. The impedance matching can be done by either designing the SRR for a given frequency to ensure a match, or using a variable impedance tuner to provide additional circuit impedance. The latter is less desirable as the tuner acts as a power sink, similar to an extra resistor in the system, making the plasma generation less efficient.

The dielectric constant of the substrate on which the microstrip structure is built on affects the resonant frequency of the resonator. The dielectric constant is also called the relative permittivity, a material property that describes the ability to store electrical energy in an electric field. A good electric

insulator with high dielectric constant is desired to minimize any leakage of current from the microstrip.

By adding an additional split ring inside the SRR, the concentric split ring resonator can be made. The second ring affects the SRR plasma properties to a large extent. The SRR produces plasma at the discharge gap making it a localized plasma. In CSRR, the plasma is distributed to both discharge gaps making it more uniformly distributed throughout the ring. But it also increases the power required to generate plasma since part of the energy is utilized to excite the second ring. CSRRs can be a better source of plasma in ion thrusters compared to the SRRs due to the evenly distributed plasma which in turn responsible for higher electron temperature. This research discusses about the impact on the plasma properties by changing the parameters of the second ring of CSRR.

2.3. SRR as a plasma source

Iza and Hopwood in 2003[17] built a low-power microwave SRR microplasma source. It operated at 900 MHz from 0.05 Torr up to 760 Torr. It was operating at less than 3 W power and at atmospheric pressure with argon. The design was fabricated on a RT/Duroid 6010.8 with a dielectric constant of 10.8. A high dielectric constant was used to reduce the wavelength of the microwave signal passing through the device which can lead to a more compact resonator structure. Further work by Hopwood and Iza in 2005 [15] studied an SRR microplasma source designed specifically for operating in air. Berglund *et al.* [1] studied an SRR that removed the dielectric and ground plane material within the gap region while operating at a higher frequency. The previous research at UAH by Dextre *et al.* analyzed the impact on plasma by changing the width of the ring of the SRR[18]. The further work compared the SRR and CSRR plasma properties[2]. The research work of Yamauchi *et al.* in 2018 used the SRR as a plasma source for miniaturized ion engine, SRRIT1 [4]. Seton *et al.* in 2019 [19] used SRR in a Xe-microplasma thruster and analyzed the plasma properties.

2.4. Ion thruster

Electrostatic plasma thrusters utilize a large electric field to accelerate ions. An example of an electrostatic propulsion device is an ion engine. An ion engine uses an electrical grid system to provide the electric field.

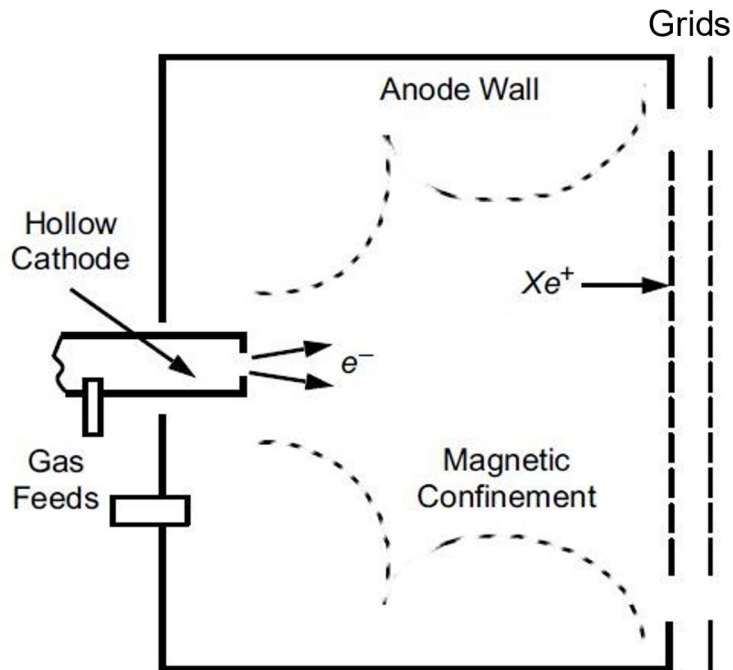


Figure 2.2. Illustration of an electron bombardment ion thruster[10]

Figure 2.2 shows an illustration of the ion thruster. The electrons are released from the hollow cathode at very high energies which bombard the neutral gas atom in the thruster chamber. If the electrons have sufficient energy, then ions are generated via impact ionization. The walls of the thruster are positively biased in order to confine the ions and prevent their loss from hitting the walls. The grids produce an electric field towards the exit that attract and accelerate the ions out. The exiting ions produce an opposing force on the thruster grids which propels the thruster forward. The thrust depends on the plasma number density and electron temperature at the grid. The grid properties such as hole size and number of holes also play a major role in thrust production. The ion thrusters have very high I_{sp} and the thrust is very low in the order of <1 mN to 1 N. Ion thrusters has been used in many space

missions. The NASA Solar Technology Application Readiness (NSTAR) ion thruster engine enabled the Deep Space-1 mission, the first spacecraft propelled primarily by ion propulsion, to travel over 163 million miles and make flybys of the asteroid Braille and the comet Borelly.[20] Ion thrusters are now being used to keep over 100 geosynchronous Earth orbit communication satellites in their desired locations, and three NSTAR ion thrusters that utilize Glenn-developed technology are enabling the Dawn spacecraft (launched in 2007) to travel deep into our solar system. Dawn is the first spacecraft to orbit two objects in the asteroid belt between Mars and Jupiter: the protoplanets Vesta and Ceres. Most recently, the Double Asteroid Redirect Mission (DART) used ion engines to propel spacecrafts to study the effect of impact deflection of asteroids for future planetary defense.

Miniaturized ion thrusters use the same physics as ion thruster but on a smaller scale. The thrust ranges from few μN to mN . CubeSats and other small satellites can use miniaturized ion thruster for orbit corrections. The plasma sources of miniaturized ion engines are the biggest challenge to their efficient operation. For traditional electron impact or bombardment ionization based ion engines, the cathode used to produce the energetic electrons typically requires higher power than the small satellites can provide. The smaller thrusters also have higher surface-to-volume ratios in the plasma chamber, which increases the ratio of surface or wall losses to the volume ionization. Thus, alternative ionization methods are needed. RF or microwave plasmas have been successfully used in ion engines. For example, Koizumi *et al.* [21] fabricated a miniature microwave discharge ion thruster which can operate at 1 W power. In this work, since SRRs work at similar low powers they could be a viable plasma source for miniaturized ion thrusters. Yamauchi *et al.* [4] from UAH fabricated a miniature ion thruster, the SRRIT-1 which used a SRR as the plasma source. The thrust was in the range of μN . In this research, a CSRR is designed and tested to produce a more uniform plasma for a miniaturized ion thruster named the SRRIT-2.

CHAPTER 3. EXPERIMENTAL METHODS

The experiment is carried out in two stages. First the fabricated CSRR is tested at 350 mTorr to obtain the resonant frequencies. The plasma number density and plasma temperature were then measured using Langmuir probes. Finally, the CSRR are tested inside a fabricated miniature ion thruster to obtain the thrust performance.

3.1. CSRR Design and Fabrication

The substrate used for fabrication of the CSRR is RT/Duroid 6010 laminate. It has a dielectric constant of 10.2. It has thin copper film on both sides which is 34- μm -thick. The material and the design was adapted from the previous research at UAH.[18]

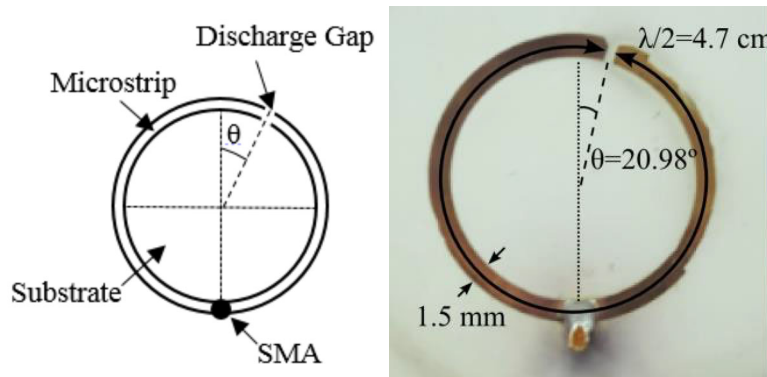


Figure 3.1. Schematic of SRR (Left) and Fabricated SRR at UAH (Right)[2]

Figure 3.1 shows the schematic design and the fabricated SRR with dimensions. One side of the copper was etched with the CSRR design using wet etching techniques. The other side was left untouched. The mean diameter of the outer ring was determined using Eq. (3.1) and Eq. (3.2).

$$c = \sqrt{\epsilon_r} \lambda f \quad (3.1)$$

$$d = \frac{\lambda}{2\pi} \quad (3.2)$$

The angle of the split on the outer ring and the distance between the outer and inner rings were determined using ANSYS HFSS (High Frequency Structure Simulation) as 20.98° from the center of the ring and 0.5 mm respectively. The split thickness was set at 500 micrometers. The

split of the inner ring lies at 180° opposite of the split in the outer ring. All CSRRs were designed for 850 MHz so the outer ring of all CSRR have same mean diameter of 1.908 cm. The width of the outer ring was set to 1.5 mm (± 0.75 mm from the mean diameter) and the inner ring width is varied between 1.5 mm, 1 mm and 2 mm (± 0.75 mm, ± 0.5 mm and ± 1 mm from the mean diameter). Figure 3.2 shows the CAD designs and the fabricated CSRRs.[22]

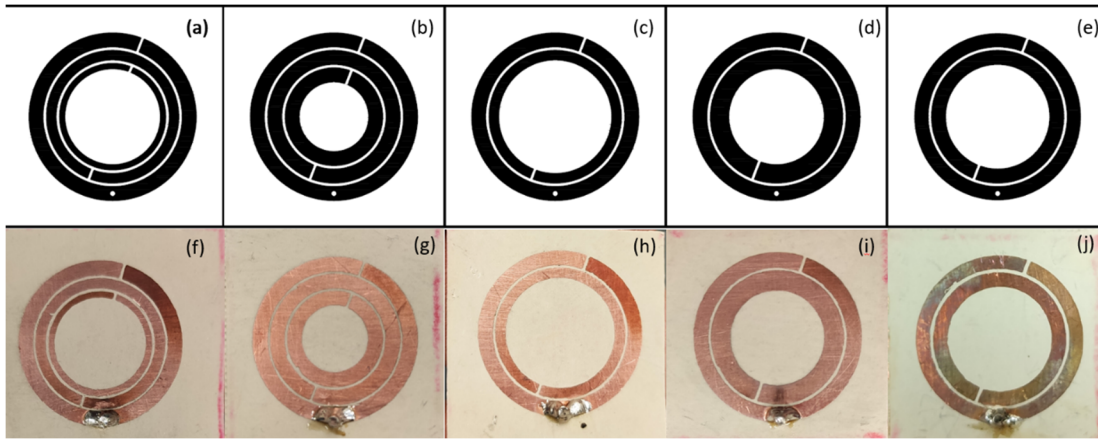


Figure 3.2. The CAD designs ((a) to (e)) and the fabricated CSRR ((f) to (j)). (a & f) 3-ringed varying width (1.5 mm, 1 mm and 0.5 mm); (b & g) 3-ringed constant width (1.5 mm all); (c & h) 2-ringed small inner (1.5 mm and 1 mm); (d & i) 2-ringed large inner (1.5 mm and 2 mm); (e & j) 2-ringed constant width CSRR.

3.2. Plasma Measurements

3.2.1. Facilities

The experiments were done in a cylindrical vacuum chamber at UAH Propulsion Research Center. The chamber has feedthroughs for propellant, electrical input/output, and pressure measurement. The gas used in the experiments was high purity argon (99.999%). For the CSRR plasma measurements, the chamber was evacuated with a mechanical pump to ~ 200 mTorr before being backfilled with argon to the working pressure of ~ 350 mTorr for all experiments. A Baratron gas independent pressure transducer was used to measure the pressure. The experimental setup arrangement is shown in Figure 3.3.

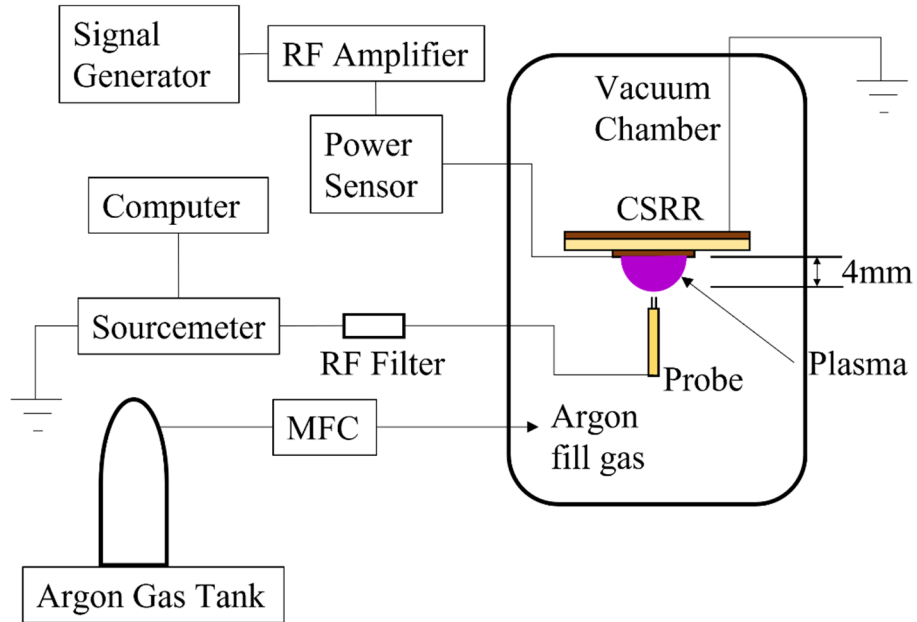


Figure 3.3. Experimental setup top-view for the CSRR plasma measurements.

The microwave signal was provided by an HP 8780a signal generator and amplified by an HPA-850 amplifier (+40 dBm, RF Bay). The output power from the signal generator was varied from -5 to 0 dBm to vary the output power to the CSRR. A digital Bird 7020 power sensor was used to measure the forward and reflected power to give the voltage standing wave ratio (VSMR) in the circuit. The forward power for all the CSRR designs at 0 dBm from the signal generator at minimum VSWR is given in Table 4.1.

The plasma generated was measured using a double Langmuir probe. The probe tip was held 4 mm away from the surface of CSRR with a two-axis Velmex linear motion stage. The probe was connected to a Keithley 2400 sourcemeter and a voltage sweep from -20 to 20 V was applied to the probe. The current data is then recorded using LabVIEW. At each voltage, a 2-point average of the current was done to reduce noise. The resulting characteristic I-V curve was then analyzed to obtain n_e and T_e . [22]

3.2.2. Double Langmuir Probe

The double Langmuir probe was fabricated by inserting two 0.1 mm diameter tungsten wires into a 2.39 mm diameter double bore alumina tube, exposing ~1 mm length of wire on the tip. The double bore alumina tube provided electrical isolation between the two wires. An external bias voltage from -20 to 20 V was applied to the Langmuir probe with a Keithley 2400 sourcemeter to attract the ions or electrons to the exposed probe tips. The current at each voltage was measured to create the characteristic I-V curve which was analyzed to determine the plasma properties.[23] Double probe theory in this experiment also requires a collisionless plasma, determined by $\alpha_c < 1$. This is necessary as the probe analysis conducted assumes a collisionless regime. The electron temperature was determined using the change in current with respect to voltage and the ion saturation currents, i_1 and i_2 [24], given as,

$$\frac{dI}{dV} = \frac{e}{kT_e} \frac{|i_1| * i_2}{|i_1| + i_2} \quad (3.3)$$

Derived from Equation (3.3) is the electron temperature given as,

$$\frac{kT_e}{e} = \frac{|i_1| * i_2}{|i_1| + i_2} \left(\frac{dI_p}{dV_p} \right)_0^{-1} \quad (3.4)$$

The plasma number density, n_i , represents the quasi-neutral ion and electron densities of the plasma. This is calculated using,

$$n_i = \frac{2I_{i,sat}}{qA \left(\frac{kT_e}{2\pi M} \right)^{\frac{1}{2}}} \quad (3.5)$$

In these equations, $I_{i,sat}$ is the average of the saturation currents, e is the magnitude of the electronic charge, m is the electronic mass, M is the ion mass, q is the electron charge, k is the Boltzmann constant, and A is the probe area [25].

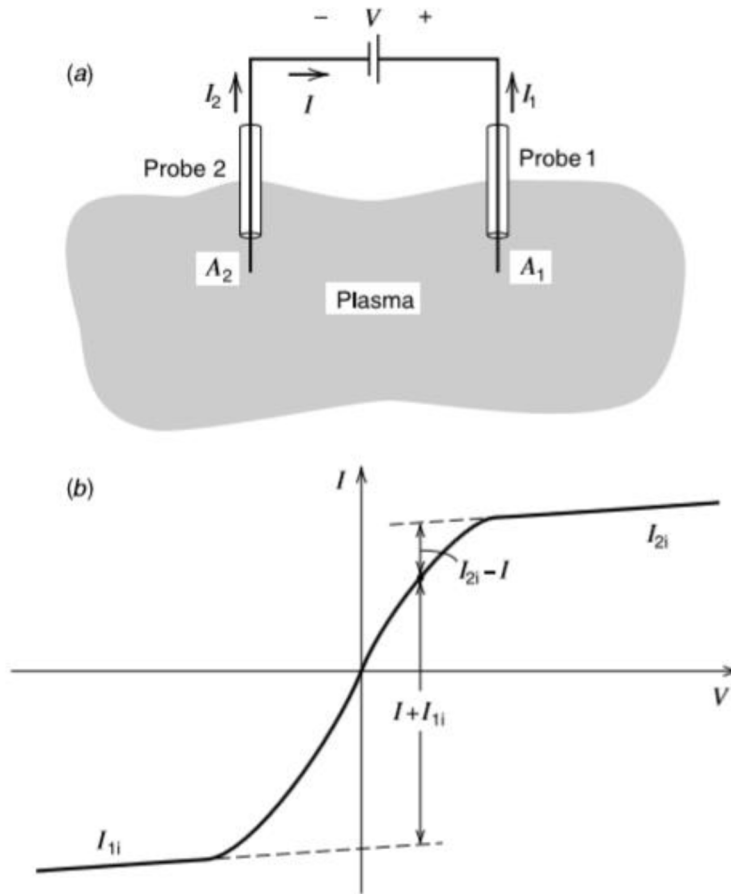


Figure 3.4. Schematic of double probe measurement. (a) voltage and current notation, (b) typical current-voltage characteristic[26]

Figure 3.4 shows a schematic of the current flow observed by the double probe when exposed to plasma. The I-V characteristic curve is obtained when applying the bias voltage on the probe tip.

The data were recorded using LabVIEW, and double probe theory can be used to determine the desired plasma properties from the data. In a double probe, only the ion saturation is observed.

In double Langmuir probe diagnostic technique, it is important to consider the electron energy distribution function (EEDF). The assumption of a Maxwellian energy distribution is made for conventional Langmuir probe theory. In Maxwellian plasmas, determining the electron temperature is not hard as the electron energy can be characterized by a single scalar quantity, T_e .

This is particularly common in space plasmas discussed by Hoegy [27]. In this research, the determination of plasma properties is also conducted with the assumption of a Maxwellian distribution for simplicity.

3.2.3. 2D Mapping and analysis

A probe mapping technique is applied to obtain plasma distribution data over the device. Using a two-axis Velmex stepper motor, a matrix of I-V curves is generated at each point of a 11x11 grid 4 mm above the resonator as shown in Figure 3.5. The plasma properties at each point are then determined. A total of 121 points were collected where each horizontal step and vertical step is 2.54 mm. [22]

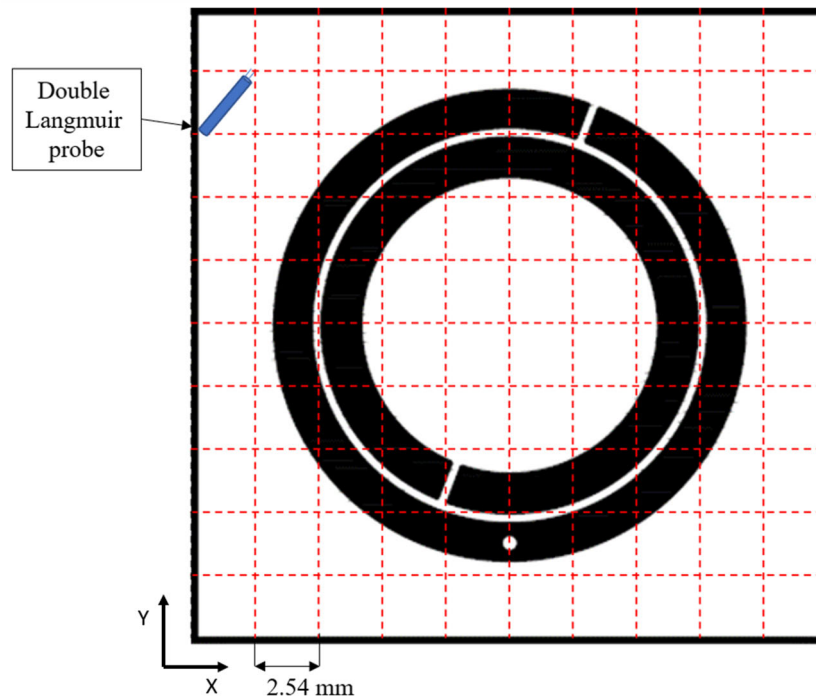


Figure 3.5. 11 x 11 grid of CSRR with probe at the 13th position

Probe mapping is most effective in understanding the size and uniformity of the device. By knowing the position of the probe on the map, the 2D surface properties of the plasma can be

obtained. Since the CSRR has more distributed plasma because of the two discharge gaps, it is more effective to measure from one corner of the resonator to the other instead of just mapping the area of the ring. The discharge gaps are expected to have more plasma than the other parts of the ring. But since there are different variations in the design the plasma distribution can be different in different designs. Each point shown on Figure 3.5. represents an I-V curve collected from the Langmuir probe.

The collected probe data is then analyzed with the help of MATLAB. The plasma number density and electron temperatures are calculated using the saturated ion current values. The T_e and n_e were calculated using Eq. (3.6) and Eq. (3.7), respectively[28].

$$T_e = \frac{|I_{max}I_{min}|}{(|I_{max}| + |I_{min}|) \left(\frac{dI}{dV}\right)_{max}} \quad (3.6)$$

$$n_e = \frac{|I_{max}I_{min}|}{(|I_{max}| + |I_{min}|)} \frac{\ln(-0.5)}{eA_p \sqrt{\frac{k_B T_e * 11600}{m_i}}} \quad (3.7)$$

3.3. Thruster Setup

The previous research at UAH by Toyofumi *et al.*[4] demonstrated the SRR as a plasma source for miniature ion thruster engine in the SSRIT-1. The miniature ion engine designed and used here along with the experimental setup was adopted from the SRRIT-1. An HCT250 heaterless cathode (Plasma Controls, LLC) was used as the neutralizer cathode. Since the CSRR generates the plasma inside the ion engine, a second ionization cathode was not needed. Figure 3.6 shows the CAD model of the thruster assembly. Figure 3.7 shows the fabricated ion engine SRRIT-2 and the neutralizer cathode setup in operation. Figure 3.8 shows the experimental setup of the ion thruster. The SRRIT-2 had a chamber length of 4 mm, *i.e.*, distance between the CSRR surface

and the screen grid. This length was chosen to place the grids approximately where the Langmuir probe measurements were taken of the CSRR. The screen grid and the accelerator grid had 271 holes each and the grid thickness was 1.27 mm. The diameter of the screen grid holes was 1.25 mm, and the accelerator grid holes was 1 mm. The grids were ~ 1 mm apart separated by electrical-insulating mica sheet. These grid changes were made to increase the efficiency of the thruster.[22]

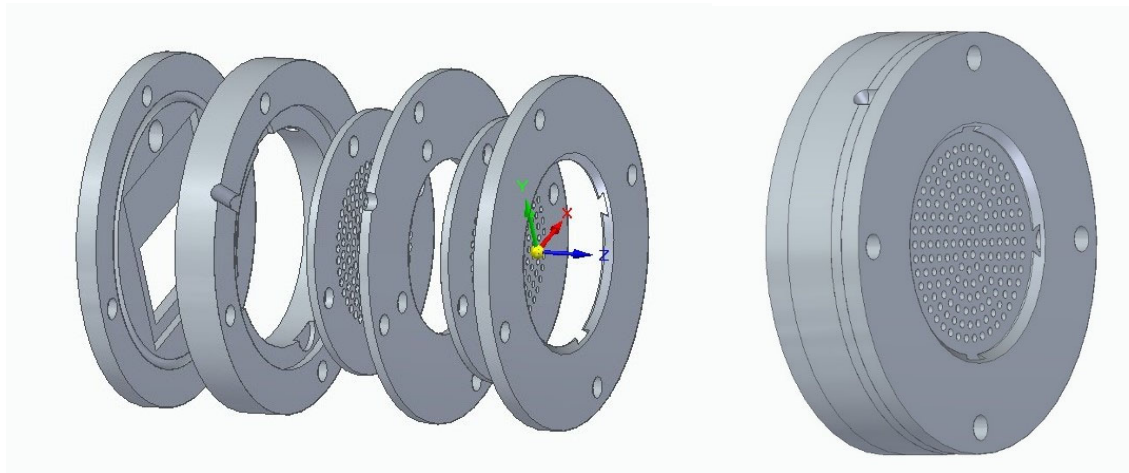


Figure 3.6. CAD model of the thruster disassembled (left) (from left to right; CSRR holder, thruster chamber, screen grid, insulator, accelerator grid and covering), and assembled isometric view(right)

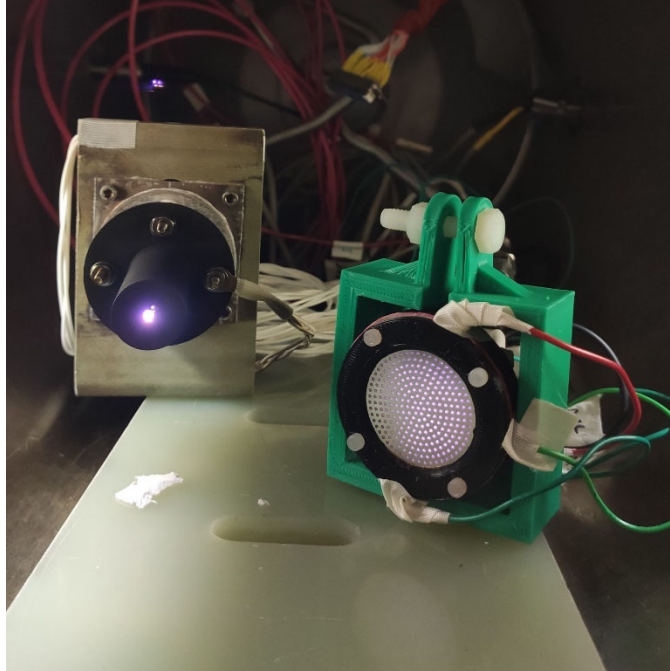


Figure 3.7. Working of the fabricated ion engine SRRIT2 (Right) and neutralizer cathode (Left) setup inside the vacuum chamber.

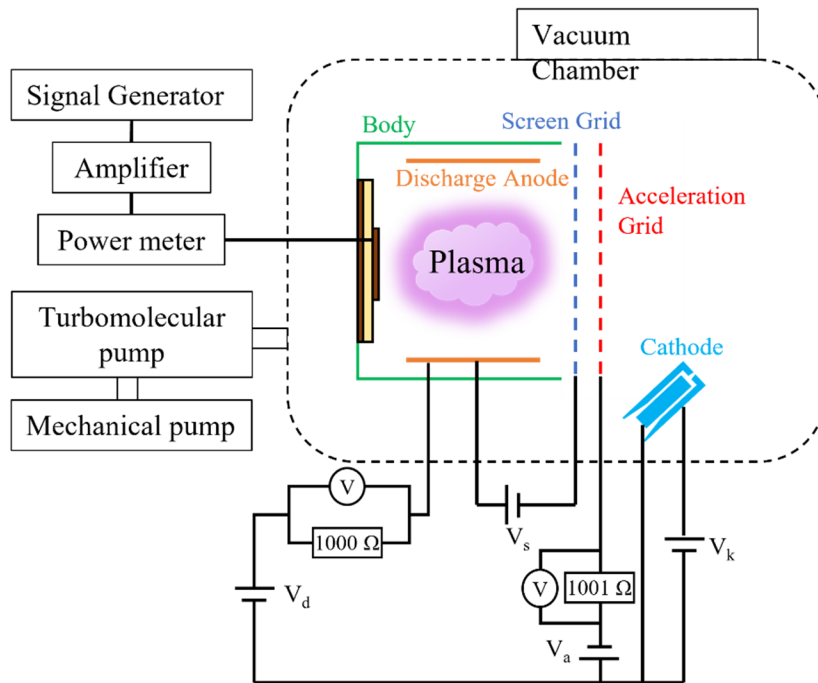


Figure 3.8. Experimental setup of ion thruster

3.4. Neutralizer Cathode

Ion thrusters must neutralize the ion beam leaving the thruster by providing electrons emitted from a cathode into the beam. Figure 3.9 shows the schematic representation of the hollow cathode. The plasma is generated due to the extreme heat inside the cathode tube and the ionized gas is propelled out through a nozzle shaped exit. The neutralizer cathode used in the SRRIT-2 is an arc start cathode developed at Colorado State University (CSU) and sold by Plasma Controls LLC. The cathode has a barium-based insert with a graphite keeper. To start the neutralizer cathode, the keeper voltage and current were initially set at 575 V and 1.5 A. Then the argon gas was “slugged” into the cathode by closing the cathode gas line valve and allowing the pressure to build up. The valve was then quickly opened to allow a high-pressure mass of argon to flow into the cathode. A 0.127 mm (0.005 in) diameter orifice was added to the cathode gas line to extend the high-pressure flow time. Once the extracted current stabilized, the final keeper voltage and current in the cathode were brought down to 75.5 V and 0.4 A and the mass flow rate was maintained at 4 SCCM.

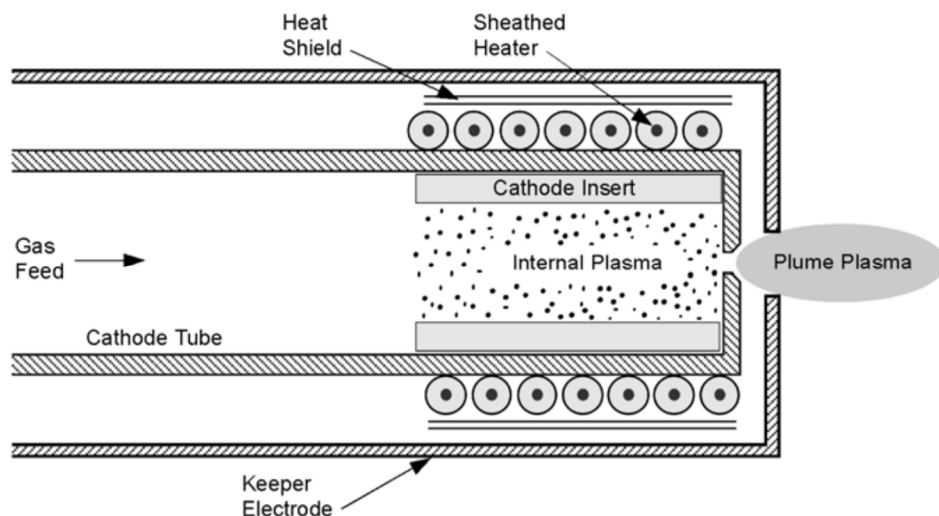


Figure 3.9. Schematic of Hollow Cathode[10]

CHAPTER 4. RESULTS AND DISCUSSION

The resonant frequency for all CSRR designs were first determined from simulations and then from experiments. The HFSS electromagnetic model calculated the antenna return loss (S11) parameter, and the frequency for minimum S11 is the simulated resonant frequency. The experimental resonant frequency was found by connecting the fabricated CSRR to the microwave power system and varying the microwave generator frequency to minimize the measured VSWR. The CSRRs were next mapped using the double Langmuir probe, and then integrated into the ion engine to measure thrust performance.

The width of the rings can change the capacitive behavior within the discharge gaps. When designing SRRs, increasing the capacitance to provide a stronger resonance is common [29]. However, an important parameter examined in ring resonators is the resonant width [30]. Explored by Bilotti [31] in multiple ring resonators, distributed capacitance in an SRR can saturate based on geometric features, including the width. The same concept applied to single SRRs and CSRRs implies that a resonant width exists where impedance is best matched with the microwave system and device couples best with the applied microwave signal.

4.1. Modeling and Test of CSRR

After the CSRRs were designed using the theoretical equations, they were modeled in HFSS to determine the simulated resonant frequencies. A frequency sweep in HFSS produces the S11 parameter plot which determines the resonant frequency is shown in Figure 4.1. Then the simulations were redone at the simulated resonant frequency to obtain the CSRR electromagnetic profile. The electric field distribution on the different CSRRs at their resonant frequencies are shown in Figure 4.2. The resonant frequency obtained from simulation are given in Table 4.1.

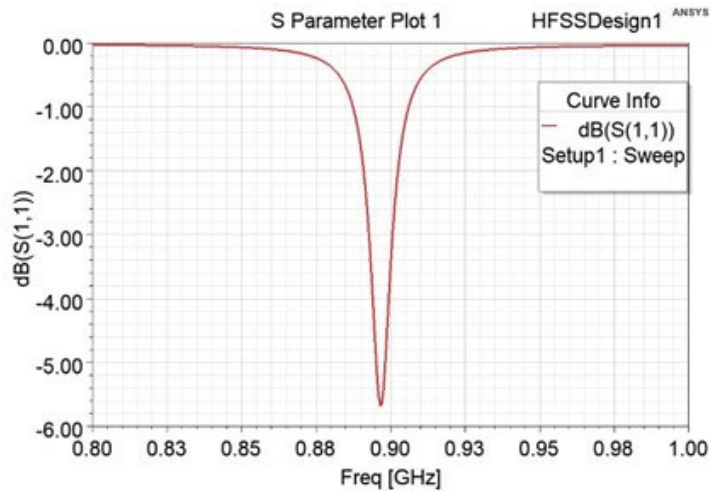


Figure 4.1. S11 plot for 3-ringed constant width CSRR

Table 4.1. Resonant frequencies

Design	Simulated Resonant Frequency	Experimental Resonant Frequency
2-ringed constant width	911 MHz	897 MHz
2-ringed small inner	888 MHz	865 MHz
2-ringed large inner	924 MHz	910 MHz
3-ringed constant width	896 MHz	875 MHz
3-ringed varying width	849 MHz	820 MHz

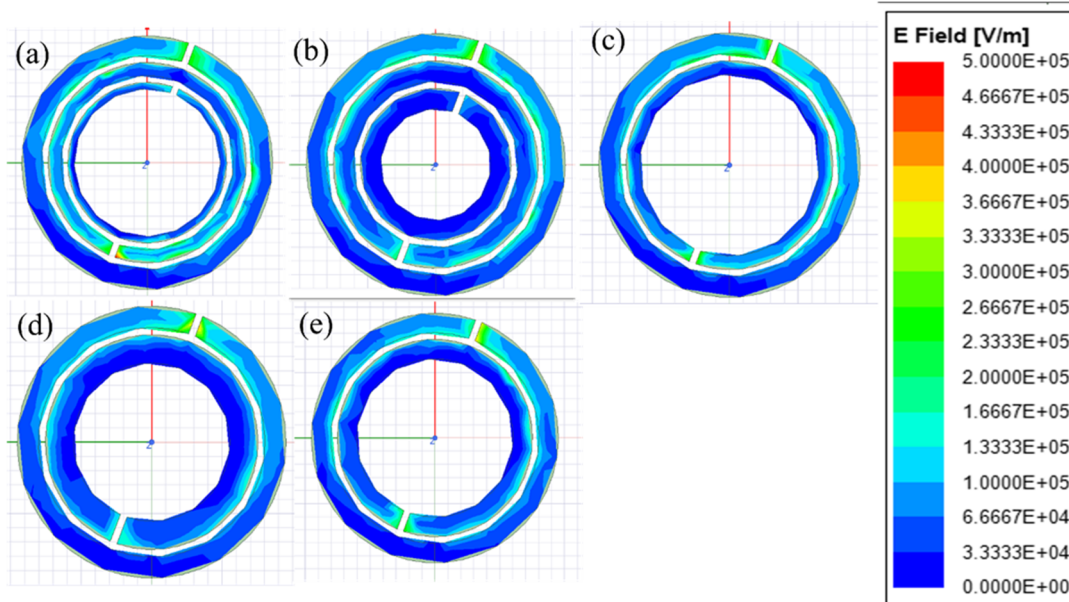


Figure 4.2. The electric field simulation for (a) 3-ringed varying width (1.5 mm, 1 mm and 0.5 mm), (b) 3-ringed constant width, (c) 2-ringed small inner (1.5 mm and 1 mm), (d) 2-ringed large inner (1.5 mm and 2 mm), (e) 2-ringed constant width CSRR.

Comparing Figure 4.2a and Figure 4.2d, it can be seen that the electric field gets more distributed throughout the CSRR with more inner rings while keeping the width of the ring constant. Figure 4.2a and Figure 4.2b show that by reducing the width of the inner ring, the electric field is distributed to the inner ring split from the outer ring split. From Figure 4.2e, by both reducing the width of the inner rings and increasing the number of rings, the electric field gets more evenly distributed throughout the CSRR. Comparing Figure 4.2a and Figure 4.2c, increasing the width of the inner ring seems to have minimal effect on the electric field.

The CSRRs were tested to obtain the experimental resonant frequencies. The tests were done at ~ 350 mTorr and at ~ 7.25 W forward power. The input frequency was varied within the theoretical range and the frequency at which the plasma is sustained with minimum VSMR was considered as the experimental resonant frequency. Pictures of the plasma generated at the resonant frequencies are shown in Figure 4.3. The bright area on the CSRR indicates regions of high plasma density. The experimental resonant frequencies of CSRR are given in Table 4.1.

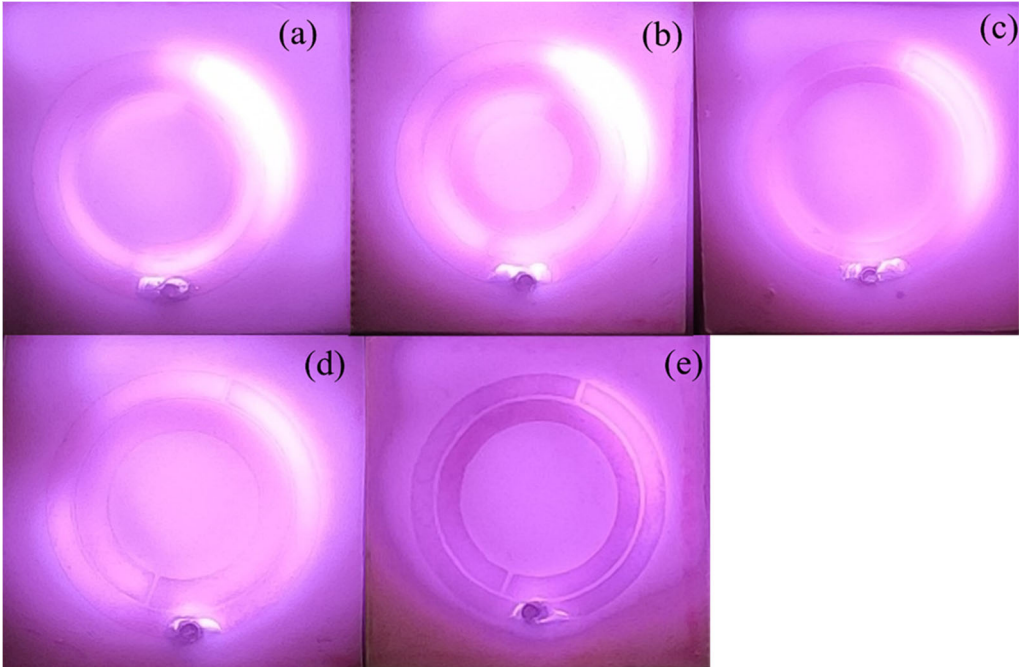


Figure 4.3. Plasma generation in (a) 3-ringed varying width (1.5 mm, 1 mm and 0.5 mm), (b) 3-ringed constant width, (c) 2-ringed small inner (1.5 mm and 1 mm), (d) 2-ringed large inner (1.5 mm and 2 mm), (e) 2-ringed constant width CSRR at 897 MHz, 865 MHz, 910 MHz, 875 MHz, 820 MHz frequencies respectively.

4.2. Plasma Mapping

The CSRR was mapped on a 11x11 grid and the I-V data at each point was measured using double Langmuir probe as shown in Figure 3.5. As example, the 3-ringed constant width CSRR results are shown in Figure 4.4. Surface plot of plasma number density of 3-ringed constant width CSRR and Figure 4.5. Surface plot of electron temperature of 3-ringed constant width CSRR. The density and temperature maps for all the designs are given in **Error! Reference source not found.** In Figure 4.4. Surface plot of plasma number density of 3-ringed constant width CSRR, the plasma number density was higher at the split region with a total number density of $\sim 3.5 \times 10^{18} / \text{m}^3$. The total number density was calculated by adding the number densities at all 121 points measured. This was done to obtain a better measure of the total number of ions produced, which can be more useful than just the peak or average value. The electron temperature from Figure 4.5. Surface plot

of electron temperature of 3-ringed constant width CSRR shows a mostly uniform distribution across the CSRR with an average electron temperature of ~ 2.3 eV, except at the lower left corner (0,10) region. The minimum and maximum number densities were $\sim 4.3 \times 10^{15} \text{ m}^{-3}$ and $\sim 7 \times 10^{16} \text{ m}^{-3}$.³ The minimum and maximum electron temperatures were ~ 1.3 eV and ~ 2.5 eV.

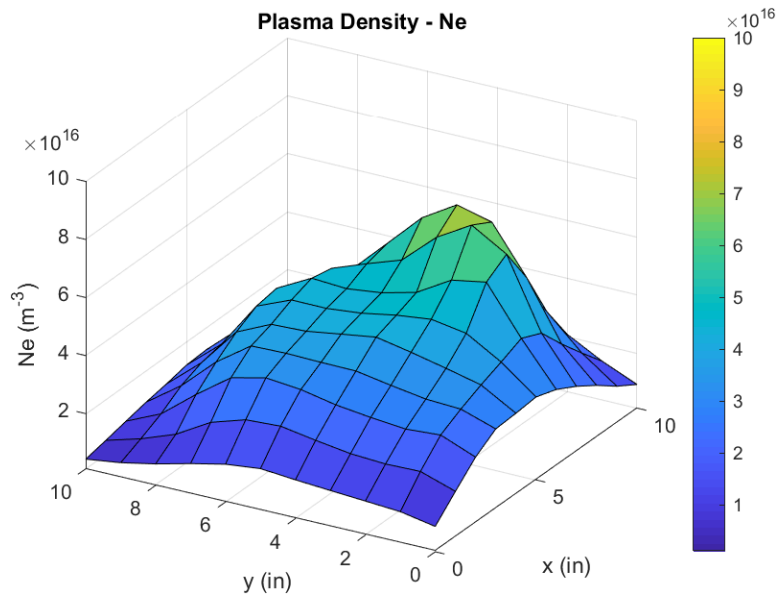


Figure 4.4. Surface plot of plasma number density of 3-ringed constant width CSRR

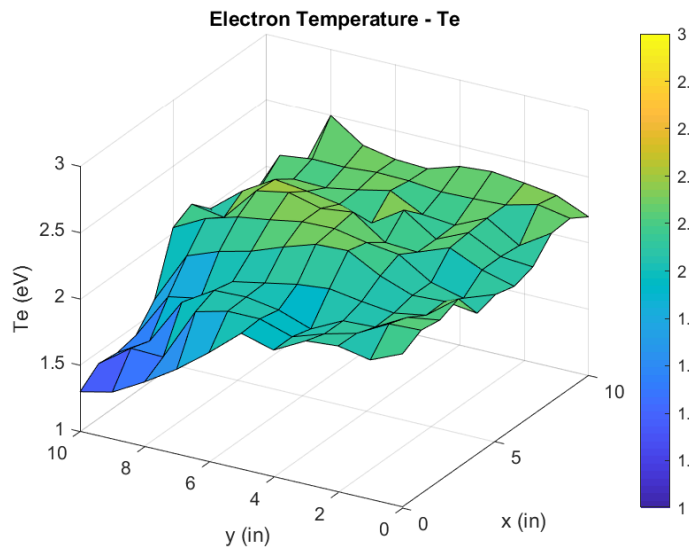


Figure 4.5. Surface plot of electron temperature of 3-ringed constant width CSRR

The data for the other ring are processed the same way as the above method and tabulated below in Table 4.2. The 2 rings constant width design is the reference for comparison. The table shows that the 2 Rings with 1 mm inner ring width has the highest density and the lowest average electron temperature. In the 3 rings constant width design, by increasing the number of the rings, the power provided to the outer ring will be shared by the inner rings thus reducing the ionization capability of the CSRR for the same amount of input power as 2 rings constant width. In the 2 rings varying inner ring width design, by reducing the width of the inner ring, the power required by the inner ring to ionize is reduced, which increases the ionization for the same amount of input power as 2 rings constant width. This is because the electric field produced by the outer ring couples with the inner ring to produce an induced EMF which in turn produces an electric field to ionize the plasma. So, the area of the inner ring determines the electric field needed from the outer ring to ionize the argon. By increasing the width of the inner ring, the power required for the inner ring to ionize increases which decreases the ionization for the same input power. The 3 rings varying width design has a decreased ionization than 2 rings constant width because of the increased number of rings and increased ionization than 3 rings constant width due to the reduced inner ring width.

Table 4.2. Measured CSRR plasma density and electron temperature results and theoretical thrust and Isp.

Design	Parameter	Experimental			Calculated	
		Total or Average	Minimum	Maximum	Thrust (mN)	I _{sp} (s)
2 Rings constant	Ne in m ⁻³ (Total)	5.4x10 ¹⁸	5.1x10 ¹⁵	1.2x10 ¹⁷	8.29	2633.8
	Te in eV (Average)	1.98	0.51	2.44		
3 Rings constant	Ne in m ⁻³ (Total)	3.6x10 ¹⁸	4.3x10 ¹⁵	7.0x10 ¹⁶	5.62	2633.8
	Te in eV (Average)	2.09	1.30	2.50		
3 Rings varying	Ne in m ⁻³ (Total)	3.9x10 ¹⁸	3.1x10 ¹⁵	7.5x10 ¹⁶	6.44	2633.8
	Te in eV (Average)	2.48	1.45	3.29		
2 Rings 1mm inner	Ne in m ⁻³ (Total)	5.6x10 ¹⁸	4.4x10 ¹⁵	1.2x10 ¹⁷	8.32	2633.8
	Te in eV (Average)	1.89	0.46	2.53		
2 rings 2mm inner	Ne in m ⁻³ (Total)	5.0x10 ¹⁸	5.1x10 ¹⁵	9.3x10 ¹⁶	8.16	2633.8
	Te in eV (Average)	2.17	0.53	3.05		

The plasma measurements would indicate that the 2 ring 1 mm inner ring width design produces the highest density plasma, which according to ion engine performance equations should produce the highest thrust. The equations for thrust and Isp for ion engines are given in Eq. (4.2) and Eq. (4.3), respectively. To do the calculations, some assumptions were made. The assumptions were 1) the screen grid transparency, T_s was considered as 0.83, 2) the grid area, A_g was considered as 7.917x10⁻⁴ m calculated based on the ion thruster model designed which is further discussed and 3) the beam voltage V_b was assumed to be 141.2 V. The beam current I_b was calculated using the Eq. (4.1). And Table 4.2 shows the calculated thrust and Isp. The beam current, thrust and the specific impulse are calculated using the following equations,

$$I_b = 0.61n_i e A_g T_s \sqrt{\frac{k_b T_e}{m_i}} \quad (4.1)$$

$$T = \gamma I_b \sqrt{\frac{2m_i V_b}{e}} \quad (4.2)$$

$$I_{sp} = \frac{\gamma}{g_0} \sqrt{\frac{2eV_b}{m_i}} \quad (4.3)$$

From Table 4.2, the calculations show that the 2 rings 1 mm inner ring width design performs better than the other designs which is due to the direct proportional nature of thrust and number density. The thrust is calculated at every point using the number density and electron temperature at that point and all the thrust values are added to provide the total thrust. Since the V_b is considered constant the I_{sp} stays constant for all designs.

4.3. Ion Thruster

For ion engine operation, the vacuum chamber was evacuated to high vacuum using a turbomolecular pump to a base pressure of 2×10^{-6} Torr. The chamber operating pressure varied from 8.29×10^{-5} Torr to 1.43×10^{-4} Torr depending on the mass flow rate of argon.

The resonance frequency of the CSRR, once inside the ion engine, shifted slightly compared to the plasma measurements. The new resonant frequencies during engine test are shown in Table 4.3. The CSRR was powered at the respective frequency and the argon gas was also slugged into the thruster to raise the pressure temporarily inside to initiate the plasma. Once the ionization starts the mass flow rate was lowered to 4 SCCM. The signal generator was initially set at 0 dBm. The anode voltage, screen grid voltage and the accelerator grid voltage were set at 151.2 V, 5 V and 30 V, respectively. These voltages were found by trial-and-error method such that it works for a wide range of forward power and mass flow rate. The mass flow rate was set as constant and the forward power on the signal generator was varied from 0 dBm to -3 dBm with a decrement of 1 dBm. Then the process was repeated for different mass flow rates from 4-10

SCCM. The current to the anode and grids were measured using shunt resistors and multimeters. Assuming that the current in the anode is equal to the ion current, the ion current goes to the screen or accelerator grid and the screen grid attracts sufficient electrons, by neglecting screen current, the beam current was then calculated with Eq. (4.4). Using the beam current value, the thrust was calculated based on the Eq. (4.2), where V_b is the difference between the anode voltage and the space potential (assumed to be 10 V) which equals to 141.2 V. The I_{sp} was calculated using Eq. (4.3) and the value was estimated as 2662 seconds.

$$I_b = I_{anode} - I_{accelerator} \quad (4.4)$$

Table 4.3. Updated Resonant Frequencies.

Design	Simulated Resonant Frequency	Stand-alone Experimental Resonant Frequency	Thruster Experimental Resonant Frequency
2-ringed constant width	911 MHz	897 MHz	922 MHz
2-ringed small inner	888 MHz	865 MHz	867 MHz
2-ringed large inner	924 MHz	910 MHz	922 MHz
3-ringed constant width	896 MHz	875 MHz	897 MHz
3-ringed varying width	849 MHz	820 MHz	836 MHz

Figure 4.6, Figure 4.7, Figure 4.8 and Figure 4.9 shows the comparison of power vs thrust plots for all CSRR designs at mass flow rate of 4, 6, 8, and 10 SCCM, respectively. From the plots the 2 rings 1 mm inner ring width design performs better in terms of thrust. At lower mass flow

rates, the 2 rings 2 mm inner ring width design and 2 ring constant width design performs almost the same. At higher mass flow rates, the 2 rings 2 mm inner ring width design perform better than 2 rings constant width design.

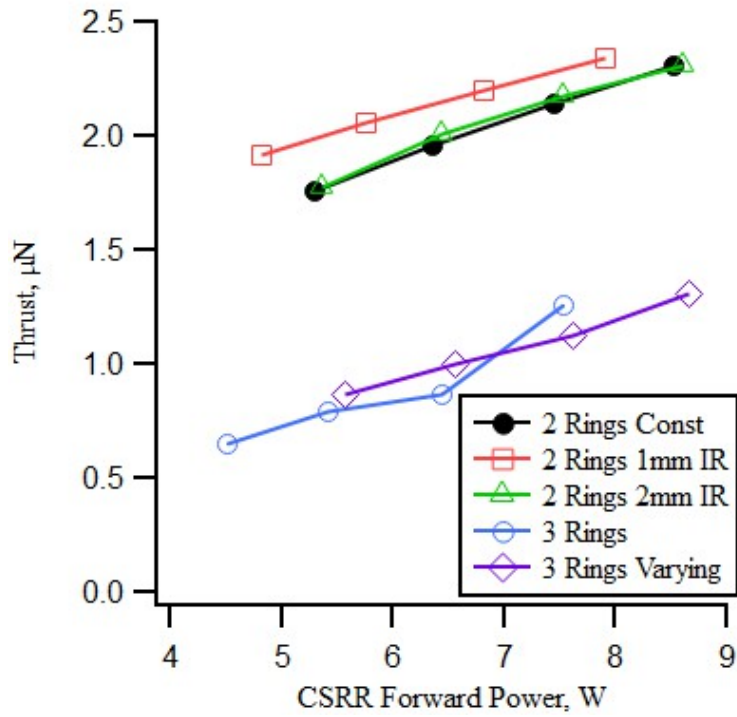


Figure 4.6. Thrust comparison plot at 4 SCCM mass flow rate.

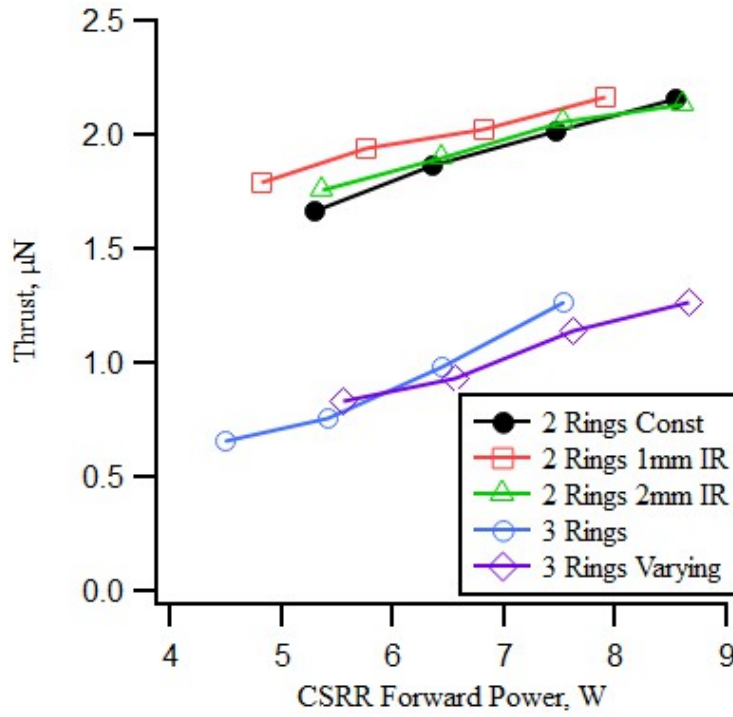


Figure 4.7. Thrust comparison plot at 6 SCCM mass flow rate.

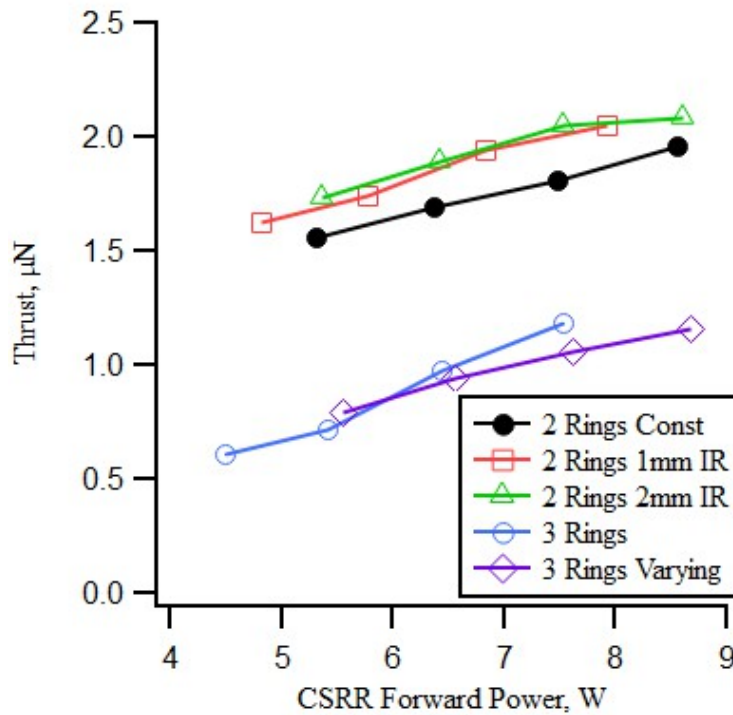


Figure 4.8. Thrust comparison plot at 8 SCCM mass flow rate.

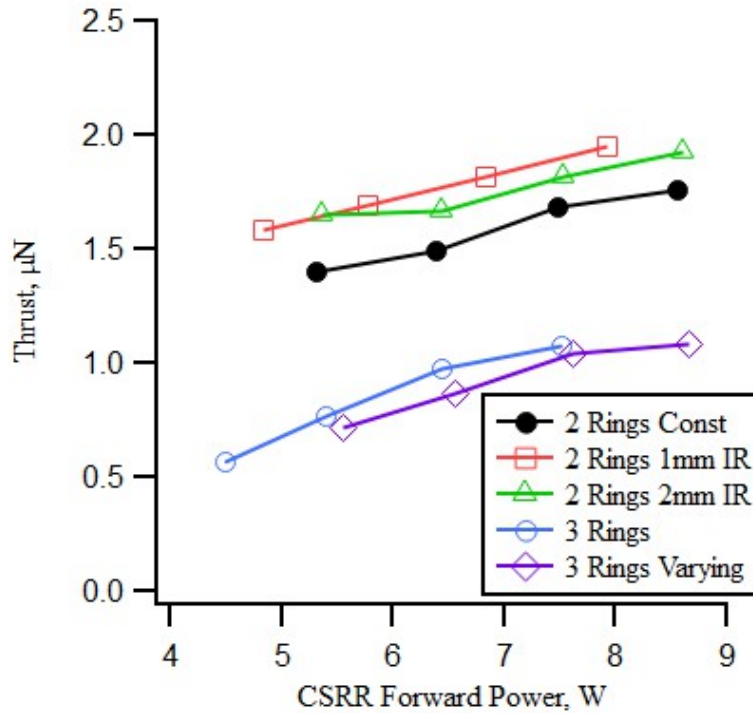


Figure 4.9. Thrust comparison plot at 10 SCCM mass flow rate.

The total operating power for the thruster was between 34.7 – 38.9 W. The power required to sustain the neutralizer cathode was 30.2 W, which was a majority of the power consumed. The remaining power, 4.5-8.7 W is consumed by the thruster for plasma generation and acceleration of the plasma. Table 4.4 shows the power breakdown for SRRIT-2. The minimum power consumed was for the 3 rings constant width design at 10 SCCM. The maximum power consumed was for the 3 rings varying width design at 8 SCCM. The thruster efficiency was calculated using Eq. (4.5) and it was found to be ~0.00007% which is extremely low for the input power and is due to the micro-Newton thrust levels. If the neutralizer cathode power is ignored the thruster efficiency changes to ~0.00035%. This low thrust is due to the screen grid transparency and the pressure inside the thruster, because the grids were designed for an average number density and temperatures. So, it was not optimized for all the designs. But compared to the SRRIT-1 the new SRRIT-2 has twice the efficiency because of the lower power consumption and better thrust.

$$\eta_T = \frac{T^2}{2\dot{m}_i P_{in}} \quad (4.5)$$

Table 4.4. Power breakdown in the SRRIT2

System	Minimum power (W)	Maximum power (W)
CSRR	4.49	8.675
Anode	0.0226	0.0453
Screen Grid	0.0005	0.0014
Acceleration Grid	0.0029	0.0057
Total	4.51	8.72

4.4. Thrust Differences from Calculated to Actual

Comparing the results from the CSRR mapping and the thruster measurements, the best design based on the performance was found to be 2 rings 1 mm inner ring width design. The thrust results of CSRR mapping calculations and the thruster measurements are different by multiple orders of magnitude. This is likely due to the reduced pressure during thruster operation compared to the mapping. The pressure inside the thruster chamber can be estimated with Eqn. (4.6), which was developed for estimating the pressure inside a hollow cathode[10]. Both a hollow cathode and the ion engine are comprised of gas flowing into a small volume and out one or more small orifices.

$$P_1 = \left(P_2 + \frac{0.78Q\zeta T_r l}{d^4} \right)^{1/2} \quad (4.6)$$

In the equation, P_1 , P_2 , Q , ζ , T_r , l , and d are upstream pressure inside the chamber in Torr, downstream pressure in Torr, flow rate in SCCM, gas viscosity in poises, temperature ratio of temperature of the gas inside the chamber to the temperature of the gas flowing in from the flow controller, length of the chamber in centimeters and diameter of the chamber in centimeters respectively. The temperature of the gas inside the chamber was assumed to be the room temperature the same as the gas flow temperature.

Table 4.5. Pressure calculation parameters and values

Variables	Values
P_2	$1.07 \cdot 10^{-4}$ Torr
Q	4 SCCM
ζ	$22.7 \cdot 10^{-5}$ poises [32]
T_r	1
l	0.4 cm
d	3.175 cm
P_1	$1.67 \cdot 10^{-3}$ Torr

The pressure was calculated for the maximum thrust case; 2 rings 1 mm inner ring at 4 SCCM. The upstream pressure of the thruster chamber was calculated to be ~ 1.67 mTorr. Since the diameter is the major factor in the equation the change in the mass flow rate will not change the pressure much unless it is in the order of 10^2 . The calculated pressure in the thruster chamber was 2 orders of magnitude less than the CSRR 2D mapping experiment chamber pressure. This shows that there was reduced density of Argon inside the thruster, which will reduce the possible plasma number density. Since the thrust and number density are directly proportional to each other, this can cause the significant difference in the thrust.

CHAPTER 5. CONCLUSION

Table 5.1 Conclusion

Research Question	Results
How do the additional rings of the CSRR affect the electric field and plasma distribution?	Additional rings reduce the electric field strength but the plasma is more uniformly distributed. The electric field strength reduction is due to the input power being constant and the surface area exposed to electric field increases with increase in number of rings
How does increasing the number of rings affect the plasma?	Increasing the number of rings decreases plasma generation. Since increasing the number of rings reduces the electric field strength the ionization decreases thus resulting in less plasma.
How does changing the width of the inner ring affect the plasma generation?	Increasing the width of the inner ring decreases the plasma generation. Increasing the width of the ring increases the area needed to be excited thus having similar negative effect as increasing the number of rings. Reduced plasma generation is the result.
	Decreasing the width of the inner ring increases the plasma generation. Decreasing the width of the ring reduced the area needed to be excited thus increasing ionization. So increased plasma generation is the result.

This work has shown that the plasma properties change on changing the geometric properties of the CSRR. Various CSRR designs have been fabricated, tested, and compared to give us the following conclusions. 1) The ionization of the CSRR increases by reducing the width of the inner rings. 2) Increasing the number of rings decreases the ionization since most of the power to the outer ring gets consumed by the inner rings for excitation. The CSRR designs were tested both stand-alone as 2D mapping and along with the thruster. The 2D mapping results shows that the 2-ringed smaller inner ring design has the maximum total thrust. This is mainly due to the maximum average plasma density of that CSRR design. The thruster results show that the same design produces more thrust which validates the 2D mapping results. The 2 rings smaller inner ring design performs better than the other designs this is due to the reduced inner ring width which

is due to the coupling of electric field with the inner ring will be more thus creating more ionization. A common thruster body was used to test all the CSRR designs.

With this understanding of the CSRR, future work can be extended to fabricate an electron extractor model using CSRR to replace the high-power neutralizer cathode. This way the total power consumption of the thruster can be reduced by a lot and also the thruster can be operated at a slightly higher pressure. In the future the thruster can also be optimized for the best design to test the limits at the best performance conditions. Few things that can be done to the thruster to improve the thrust are optimizing the grids to get the maximum perveance and achieving maximum effective grid transparency

REFERENCES

- [1] Berglund, M., Grudén, M., Thornell, G., and Persson, A. “Evaluation of a Microplasma Source Based on a Stripline Split-Ring Resonator.” *Plasma Science and Technology*, Vol. 22, No. 5, 2013. <https://doi.org/10.1088/0963-0252/22/5/055017>.
- [2] Dextre, R. “Plasma Characterization of a Single and Double Split Ring Resonator for Micropropulsion.” 2018.
- [3] Foust, J. “Despite Technical Glitches, the Company Plans to Launch the First of Nearly 12,000 Satel- Lites in 2019.” *IEEE Spectrum*, Vol. 56, 2019, pp. 50–51.
- [4] Yamauchi, T., and Xu, K. G. “A Miniature Ion Thruster Using Split Ring Resonator Microplasma.” *2018 Joint Propulsion Conference*, 2018, pp. 1–7. <https://doi.org/10.2514/6.2018-4651>.
- [5] Gott, R. P., Miller, S. D., Hodges, J. C., and Xu, K. G. “Plasma-Based Water Purification for Crewed Space Missions: Laboratory Experimental Comparisons for on-Board Applicability.” *Advances in Space Research*, Vol. 68, No. 3, 2021, pp. 1591–1600. <https://doi.org/10.1016/j.asr.2021.04.001>.
- [6] Unruh, E., Spaulding, M., Lineberry, D., Xu, K. G., and Frederick, R. “Development of an Optically Accessible Racetrack-Type Rotating Detonation Rocket Engine.” *AIAA Propulsion and Energy 2020 Forum*, 2020, pp. 1–16. <https://doi.org/10.2514/6.2020-3868>.
- [7] McCracken, G. M. “Plasma Surface Interactions in Controlled Fusion Devices.” *Nuclear Fusion*, Vol. 37, No. 3, 1997, pp. 427–429. <https://doi.org/10.1088/0029-5515/37/3/413>.
- [8] Gay-Mimbrera, J., García, M. C., Isla-Tejera, B., Rodero-Serrano, A., García-Nieto, A. V., and Ruano, J. “Clinical and Biological Principles of Cold Atmospheric Plasma Application in Skin Cancer.” *Advances in Therapy*, Vol. 33, No. 6, 2016, pp. 894–909. <https://doi.org/10.1007/s12325-016-0338-1>.
- [9] Pourali, M. “Application of Plasma Gasification Technology in Waste to Energy-Challenges and Opportunities.” *IEEE Transactions on Sustainable Energy*, Vol. 1, No. 3, 2010, pp. 125–130. <https://doi.org/10.1109/TSTE.2010.2061242>.
- [10] Goebel, D. M., and Katz, I. “Fundamentals of Electric Propulsion: Ion and Hall Thrusters.” *Fundamentals of Electric Propulsion: Ion and Hall Thrusters*, 2008, pp. 1–507. <https://doi.org/10.1002/9780470436448>.
- [11] Gay-Balmaz, P., and Martin, O. J. F. “Electromagnetic Resonances in Individual and Coupled Split-Ring Resonators.” *Journal of Applied Physics*, Vol. 92, No. 5, 2002, pp. 2929–2936. <https://doi.org/10.1063/1.1497452>.
- [12] Sauviac, B., Simovski, C. R., and Tretyakov, S. A. “Double Split-Ring Resonators: Analytical Modeling and Numerical Simulations.” *Electromagnetics*, Vol. 24, No. 5, 2004, pp. 317–338. <https://doi.org/10.1080/02726340490457890>.

- [13] P. Papadakis, A. “Microplasmas: A Review.” *The Open Applied Physics Journal*, Vol. 4, No. 1, 2012, pp. 45–63. <https://doi.org/10.2174/1874183501104010045>.
- [14] Hopwood, J., Iza, F., Coy, S., and Fenner, D. B. “A Microfabricated Atmospheric-Pressure Microplasma Source Operating in Air.” *Journal of Physics D: Applied Physics*, Vol. 38, No. 11, 2005, pp. 1698–1703. <https://doi.org/10.1088/0022-3727/38/11/009>.
- [15] Iza, F., and Hopwood, J. “Split-Ring Resonator Microplasma: Microwave Model, Plasma Impedance and Power Efficiency.” *Plasma Sources Science and Technology*, Vol. 14, No. 2, 2005, pp. 397–406. <https://doi.org/10.1088/0963-0252/14/2/023>.
- [16] Gregório, J., Alves, L. L., Leroy, O., Leprince, P., and Boisse-Laporte, C. “Microwave Microplasma Sources Based on Microstrip-like Transmission Lines.” *European Physical Journal D*, Vol. 60, No. 3, 2010, pp. 627–635. <https://doi.org/10.1140/epjd/e2010-00237-x>.
- [17] Iza, F., and Hopwood, J. A. “Low-Power Microwave Plasma Source Based on a Microstrip Split-Ring Resonator.” *IEEE Transactions on Plasma Science*, Vol. 31, No. 4 I, 2003, pp. 782–787. <https://doi.org/10.1109/TPS.2003.815470>.
- [18] Dextre, R. A., and Xu, K. G. “Effect of the Split-Ring Resonator Width on the Microwave Microplasma Properties.” *IEEE Transactions on Plasma Science*, Vol. 45, No. 2, 2017, pp. 215–222. <https://doi.org/10.1109/TPS.2016.2646661>.
- [19] Seton, R., Stureson, P., and Persson, A. “Investigating the Plasma Properties of a Xe-Microplasma Thruster.” *Journal of Physics: Conference Series*, Vol. 1319, No. 1, 2019. <https://doi.org/10.1088/1742-6596/1319/1/012013>.
- [20] Polk, J. E., Kakuda, R. Y., Anderson, J. R., Brophy, J. R., Rawlin, V. K., Patterson, M. J., Sovey, J., Hamley, J., Polk, J. E., Kakuda, R. Y., Anderson, J. R., Brophy, J. R., Rawlin, V. K., and Patterson, M. J. “AIAA 99-2274 Validation of the NSTAR Ion Propulsion System on the Deep Space One Mission : Overview f .., and Initial Results Pasadena CA 91109 35th AIAA / ASME / SAE / ASEE Joint Propulsion Conference and Exhibit Validation of the NSTAR Ion Propulsion S.” No. June, 1999.
- [21] Koizumi, H., and Kuninaka, H. Performance Evaluation of a Miniature Ion Thruster U1 with a Unipolar and Bipolar Operation. 2011.
- [22] Nagarajan, N., and Xu, K. G. “Effect of the Width and Number of Rings of Concentric Split Ring Resonator on Plasma Generation for Miniature Ion Thruster.” *AIAA Propulsion and Energy Forum*, 2021, pp. 1–13. <https://doi.org/10.2514/6.2021-3418>.
- [23] Smy, P. R. “The Use of Langmuir Probes in the Study of High Pressure Plasmas.” *Advances in Physics*, Vol. 25, No. 5, 1976, pp. 517–553. <https://doi.org/10.1080/00018737600101442>.
- [24] Sheridan, T. E., and Goree, J. “Collisional Plasma Sheath Model.” *Physics of Fluids B*, Vol. 3, No. 10, 1991, pp. 2796–2804. <https://doi.org/10.1063/1.859987>.

- [25] Cox, T. I., Deshmukh, V. G. I., Hope, D. A. O., Hydes, A. J., Braithwaite, N. S. J., and Benjamin, N. M. P. "The Use of Langmuir Probes and Optical Emission Spectroscopy to Measure Electron Energy Distribution Functions in RF-Generated Argon Plasmas." *Journal of Physics D: Applied Physics*, Vol. 20, No. 7, 1987, pp. 820–831. <https://doi.org/10.1088/0022-3727/20/7/002>.
- [26] Kim, J., and Terashima, K. "2.45 GHz Microwave-Excited Atmospheric Pressure Air Microplasmas Based on Microstrip Technology." *Applied Physics Letters*, Vol. 86, No. 19, 2005, pp. 1–3. <https://doi.org/10.1063/1.1926411>.
- [27] Hoegy, W. R., and Brace, L. H. "Use of Langmuir Probes in Non-Maxwellian Space Plasmas." *Review of Scientific Instruments*, Vol. 70, No. 7, 1999, pp. 3015–3024. <https://doi.org/10.1063/1.1149862>.
- [28] Chen, F. F. Electric Probes. In *Plasma Diagnostic Techniques*, Academic Press Inc., New York, 1965, pp. 113–119.
- [29] Horestani, A. K., Fumeaux, C., Al-Sarawi, S. F., and Abbott, D. "Split Ring Resonators with Tapered Strip Width for Wider Bandwidth and Enhanced Resonance." *IEEE Microwave and Wireless Components Letters*, Vol. 22, No. 9, 2012, pp. 450–452. <https://doi.org/10.1109/LMWC.2012.2211341>.
- [30] Resonators, S. R. "Ring Resonators : Theory and Modeling." 1969.
- [31] Bilotti, F., Toscano, A., and Vegni, L. "Design of Spiral and Multiple Split-Ring Resonators for the Realization of Miniaturized Metamaterial Samples." *IEEE Transactions on Antennas and Propagation*, Vol. 55, No. 8, 2007, pp. 2258–2267. <https://doi.org/10.1109/TAP.2007.901950>.
- [32] Huber, M. L., and Harvey, A. H. "Viscosity of Gases." 2010, pp. 229–230.

APPENDIX A: SURFACE PLOT

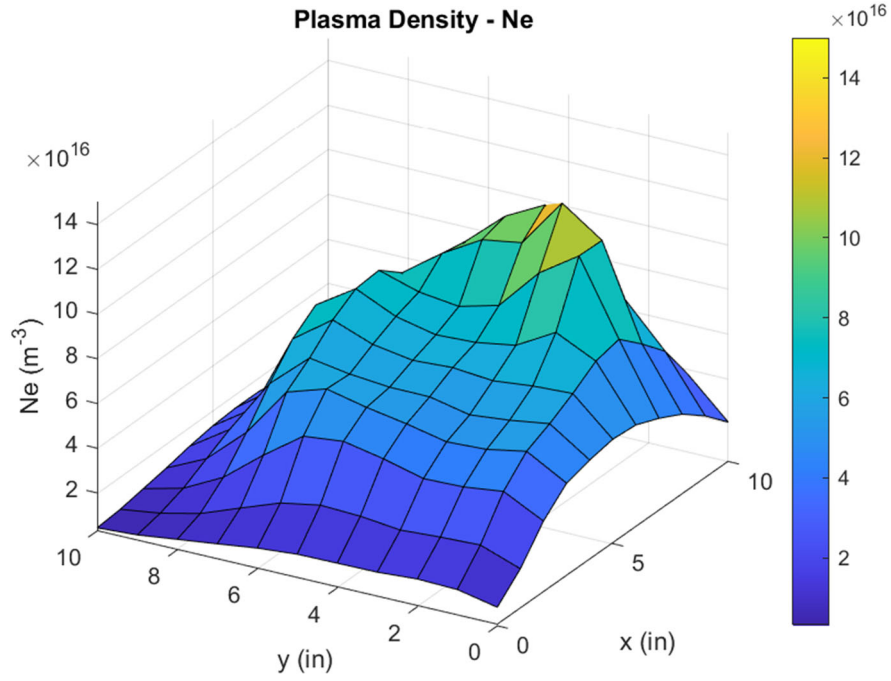


Figure A.1. Surface plot of plasma number density of 2-ringed 1 mm inner ring width CSRR

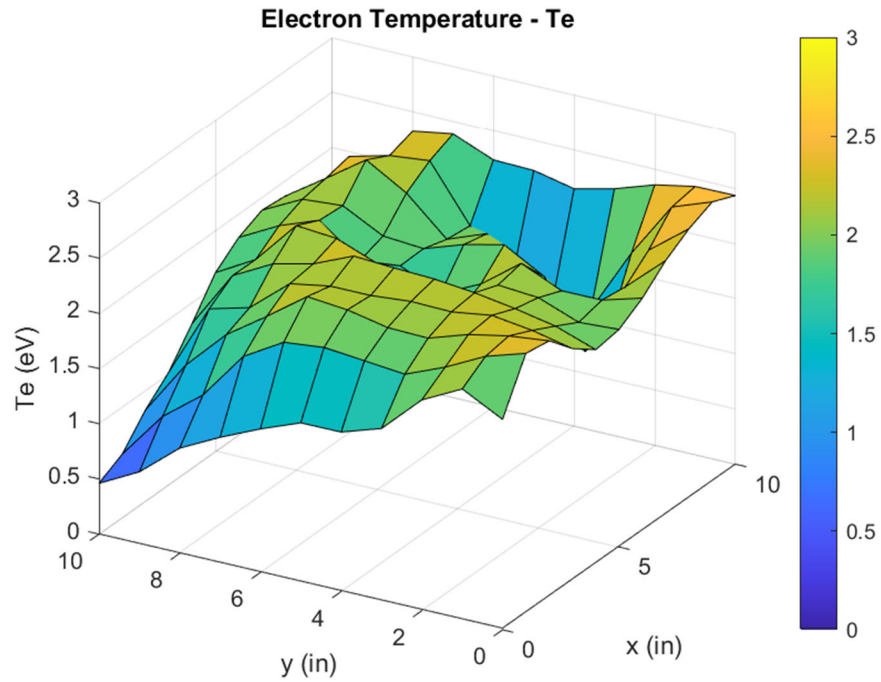


Figure A.2. Surface plot of electron temperature of 2-ringed 1 mm inner ring width CSRR

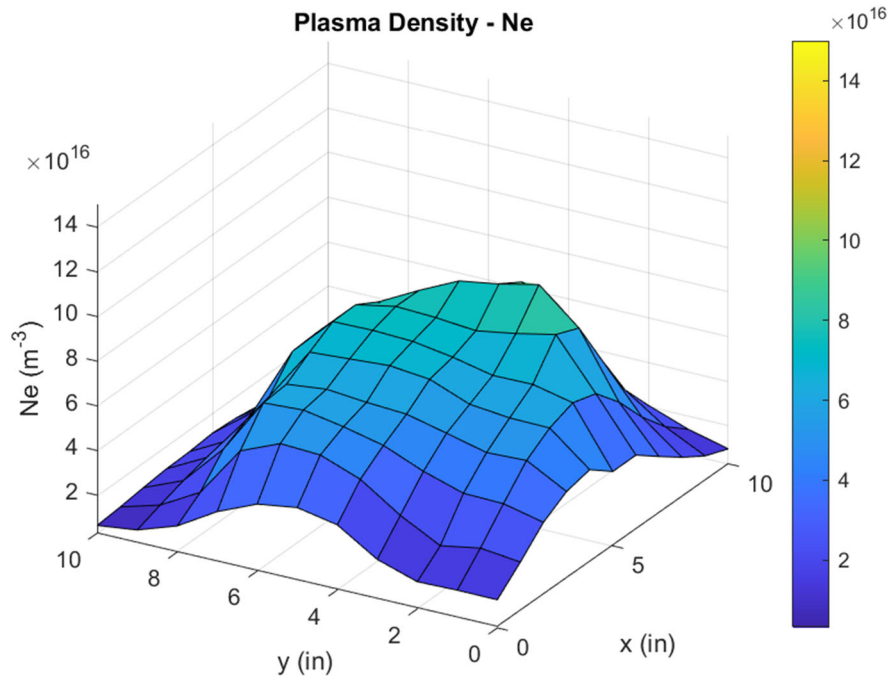


Figure A.3. Surface plot of plasma number density of 2-ringed 2 mm inner ring width CSRR

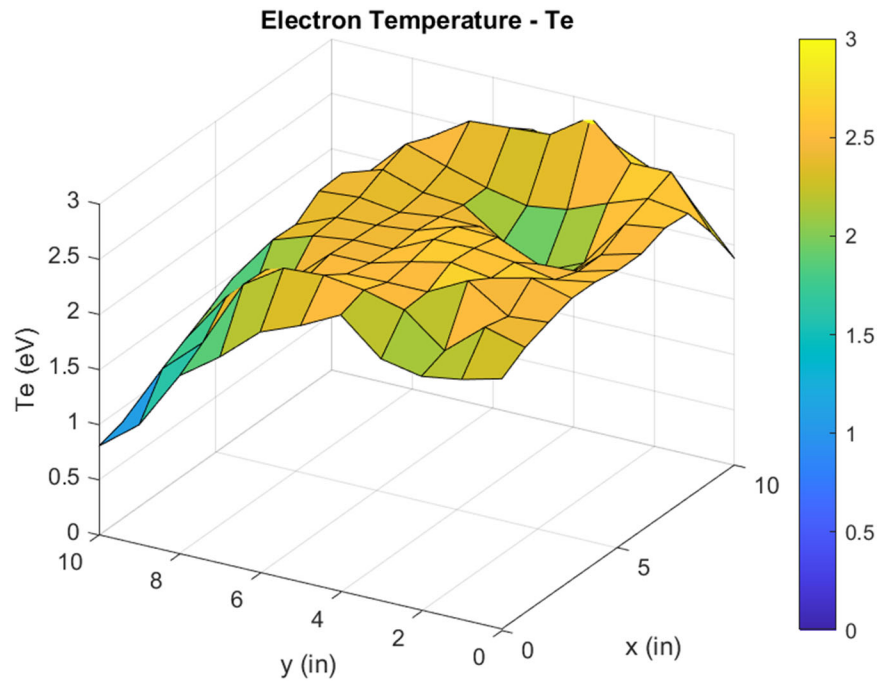


Figure A.4. Surface plot of electron temperature of 2-ringed 2 mm inner ring width CSRR

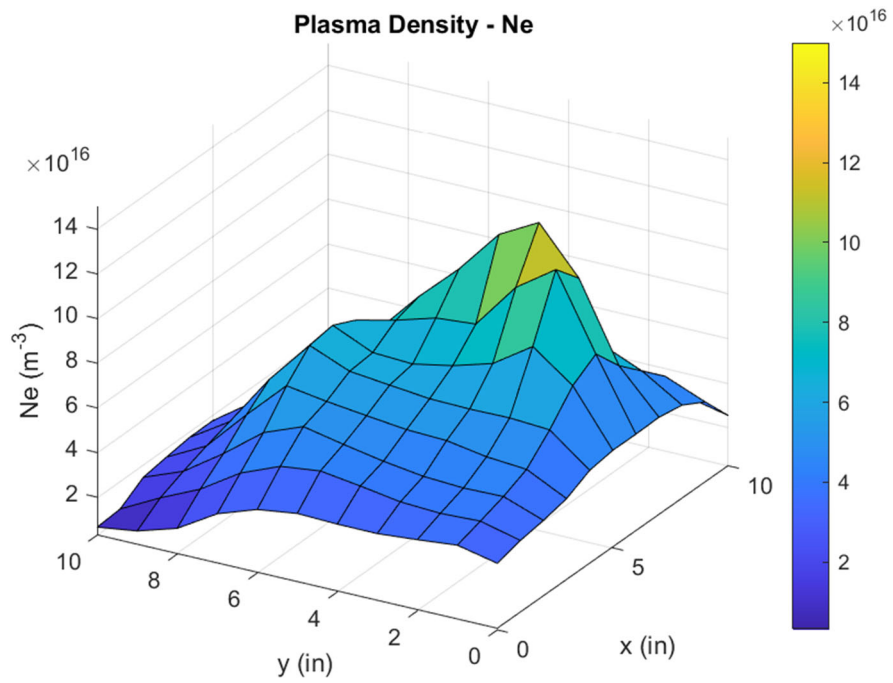


Figure A.5. Surface plot of plasma number density of 2-ringed constant width CSRR

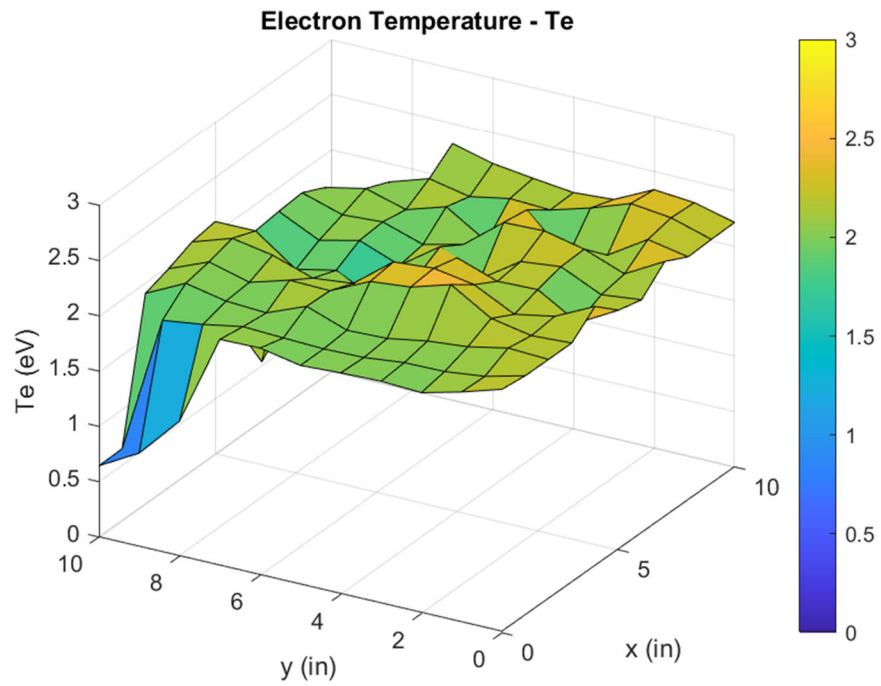


Figure A.6. Surface plot of electron temperature of 2-ringed constant width CSRR

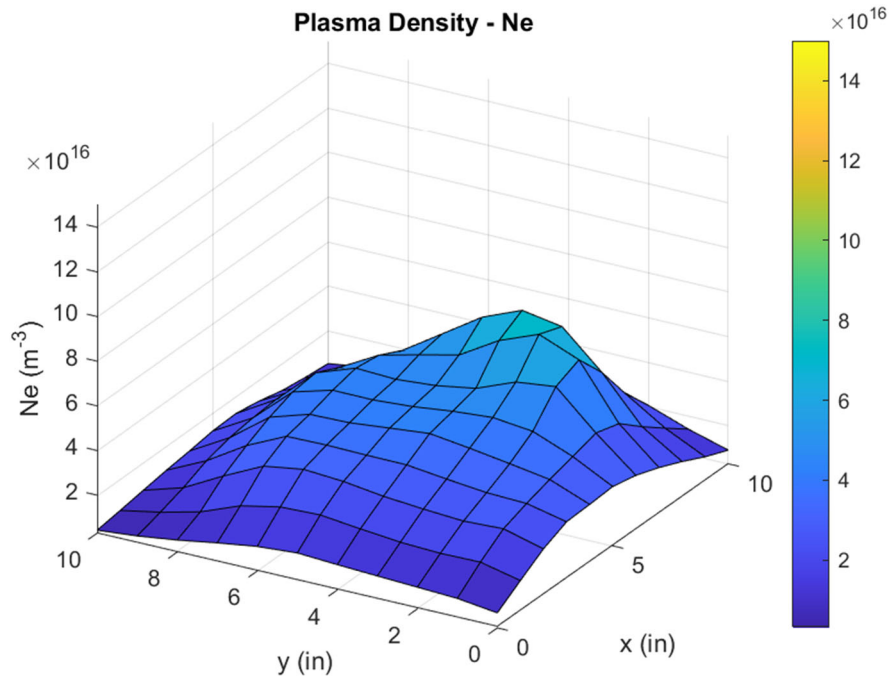


Figure A.7. Surface plot of plasma number density of 3-ringed constant width CSRR

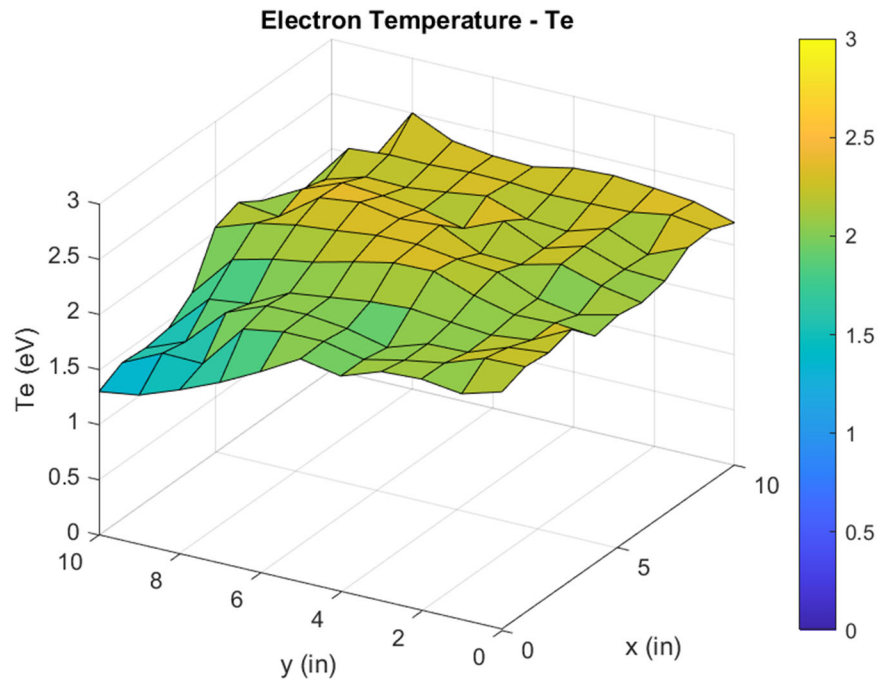


Figure A.8. Surface plot of electron temperature of 3-ringed constant width CSRR

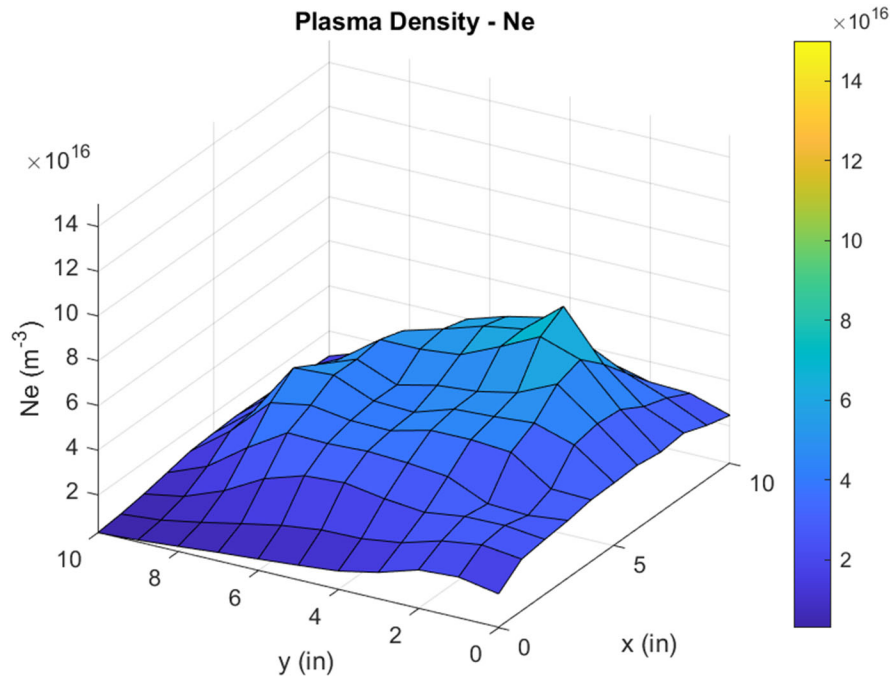


Figure A.9. Surface plot of plasma number density of 3-ringed varying width CSRR

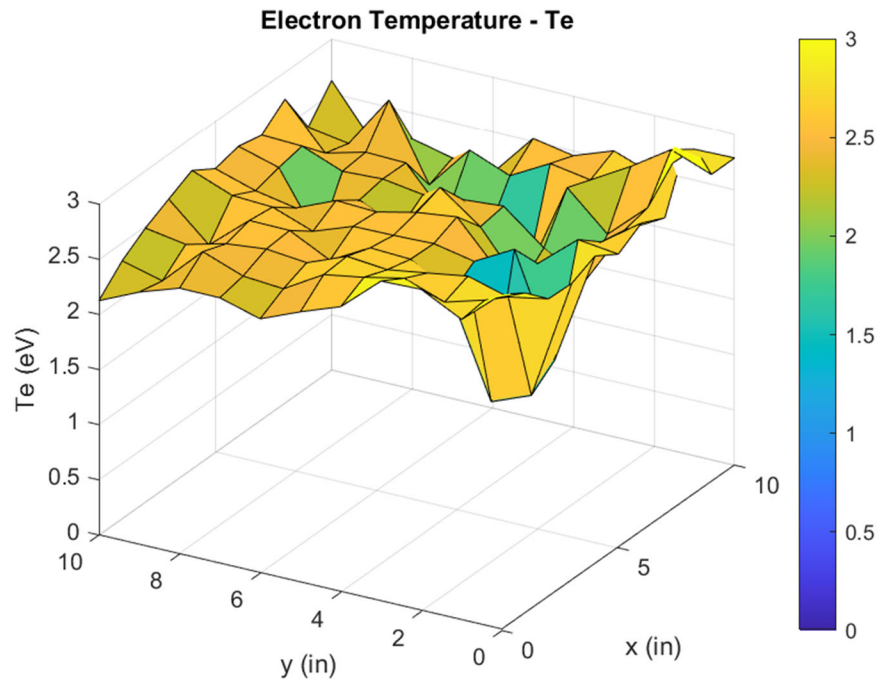


Figure A.10. Surface plot of electron temperature of 3-ringed varying width CSRR